Science Advances
AAAS

Supplementary Materials for

Recycled selenium in hot spot–influenced lavas records ocean-atmosphere oxygenation

Aierken Yierpan*, Stephan König*, Jabrane Labidi, Ronny Schoenberg

*Corresponding author. Email: aierken.yierpan@uni-tuebingen.de (A.Y.); skonig@gmx.de (S.K.)

This PDF file includes:

Supplementary Materials and Methods
Sections S1 to S6
Figs. S1 to S8
Tables S1 to S3
References

Supplementary Materials and Methods

Geochemical background of the samples

The studied MORB glasses are dredged from the southern (44°–53°S, S-MAR; $N = 16$) and northern (51°–52°N, N-MAR; $N = 2$) sections of the MAR during the *R/V Maurice Ewing* cruise EW93-09 and *R/V Trident* cruise TR138, respectively (*23, 49-51*). Locations of the samples, mantle plumes, and relevant first-order tectonic discontinues (fracture zones) are shown in Fig. S2. All these basalts were well-characterized in terms of radiogenic isotopes (Sr, Nd, Hf, and Pb) (*22, 23, 51, 52*) (Fig. 2), noble gas (*53, 54*), S isotopes (*15*), and major and trace element abundances (*24, 50, 55-57*) (Fig. S3), and therefore the selected sample suite is ideal for investigating the influence of crustal recycling on the Se isotope signature of the mantle. The most prominent feature in the S-MAR is the localized interaction between the ambient asthenospheric mantle and two mantle plumes: the off-axis Discovery plume centered at ~44.45°S, 6.45°W (~425 km away from the ridge) and the on-axis Shona plume centered between ~50°–52.5°S, 6°W (*23, 49*) (Fig. S2). A variety of recycled components have been suggested to be incorporated in these mantle plumes based on radiogenic isotope ratios (Fig. 2; see references above). Four distinct groups of S-MAR basalts can be identified: 1) depleted MORB ($N = 2$) from ridge segments unaffected by plumes; 2) Discovery anomaly ($N = 7$) showing EM1 affinity with $^{87}Sr/^{86}Sr$ ratios up to 0.705728; 3) LOMU (low-µ, µ = $^{238}U/^{204}Pb$) anomaly ($N = 3$) genetically linked to the Discovery plume but showing lower $^{206}Pb/^{204}Pb$ compared to Discovery anomaly basalts; 4) Shona anomaly ($N = 4$) with both EM1 and HIMU/high-µ affinities (most clearly seen in $^{206}Pb/^{204}Pb$–$^{87}Sr/^{86}Sr$ space; Fig. 2). The 49°S and 50°S fracture zones mark the boundaries between samples affected by the Discovery plume and Shona plume, whereas the Agulhas fracture zone offsets the Discovery anomaly samples (*49*) (Fig. S2). In addition, the N-MAR samples ($N = 2$) are depleted MORBs from a restricted ridge segment that displays one of the most remarkable depletion signatures in the mantle (*51*) (Fig. 2; Fig. S2). All these MORBs show a correspondingly wide range in their incompatible trace element compositions, with the primitive mantle-normalized $(La/Sm)_N$ ratios of 0.457–0.643 for depleted MORBs and 0.670–2.681 (mostly >1) for MORBs associated with plume enrichment (Fig. S3). On a large scale, the South Atlantic ambient depleted mantle is more enriched than the Pacific/North Atlantic depleted mantle due to the pervasive mantle pollution with DUPAL- or Indian Ocean-type mantle components (*22-24*) (Fig. 2).

The well-characterized granitoid samples (Cordilleran-type) are from the Västervik area in the southeast Sweden, which is located between two main tectonic domains, Transscandinavian Igneous Belt and Svecofennian domain, in the Baltic (*58, 59*). They have intrusion ages of ~1.8 Ga (*58*) and may provide first insights into the Se isotope composition of the Proterozoic upper continental crust.

Sample dissolution and chromatographic purification

The MORB samples used for analyses are visually fresh glass fragments (~5–15 mm). Samples were first crushed into ~1–5 mm small chips in an agate mortar and further inspected for freshness under a binocular microscope. They were successively cleaned with 18.2 MΩ·cm H_2O and ethanol in an ultrasonic bath for 15 min before they were powdered in the agate mortar. The mortar was always cleaned twice with quartz (*pro analysi*, Merck) and ethanol before each use. Sample powder was digested according to the protocols described previously (*41*). Briefly, small amounts of sample unknowns (10–15 mg MORB and ~100 mg granitoid) were first analyzed for their Se contents via isotope dilution method after a simple dissolution and single-stage chemical separation procedure [e.g., (*21, 60, 61*)]. About 190–1500 mg sample powders (MORBs, granitoids, and rock standards; Tables S1 and S2) were then mixed with adequate amounts of ^{74}Se–^{77}Se and ^{125}Te spikes and dissolved in a mixture of HF–HNO_3 at 85 °C. This was followed by evaporation at 65 °C and multiple successive treatments with HCl (heating at 130 °C and complete evaporation at 85 °C) in order to maximize Ge removal as $GeCl_4$ (*41*). Although there is concomitant Se loss in HCl matrix at temperatures higher than ~60 °C (*41, 42*), quantitative elimination of Ge is necessary because it is the major matrix-related isobaric interference.

The Se separation was performed via anion and cation exchange chromatography using 7 mL of new and pre-cleaned AG1-X8 and AG 50W-X8 resins (100–200 mesh, Eichrom). Two different protocols were followed in the anion column, namely 'HCl chemistry' and 'HF chemistry' (Tables S1 and S2). The 'HCl chemistry' was described in detail by (*41*). Briefly, the dried-down samples were loaded onto the columns in 4 N HCl. Se and most matrix elements are eluted, whereas Fe and Te are retained in the resin. After eluting Fe with 2 N HCl–5 N HF mixture, Te was collected in 0.4 N HCl. The new 'HF chemistry' developed in this work was modified from the Ge purification procedure of Rouxel *et al.* (*62*). Dry samples (after HCl evaporation) were first converted into fluoride form by dissolution and evaporation in 1 mL 27 N HF at 65 °C. They were then taken up in 5 mL 1 N HF and centrifuged to separate the supernatant and insoluble fluorides, which contain large proportions of Mg, Al, Ca, and other trace elements (*62, 63*) but not Se (*41*). After conditioning the resin with 10 mL 1 N HF, the supernatant solutions were loaded onto the columns, followed by addition of 9 mL 1 N HF. Selenium and some matrix fractions (Fe, alkalis, and some transition metals such as Co, Ni, and Cu) were eluted, whereas Ge, Al, and Ti were retained (*62*) (this work). The Se cuts (14 mL 1 N HF) were finally evaporated at 65 °C. Subsequent to the first-stage separation following these two protocols, all Se cuts were further purified using the cation resin with 0.1 N HNO_3 following (*41*). Samples processed through the 'HF chemistry' generally yielded Se recoveries of ~35–80%, overall lower compared to the 'HCl chemistry' [mostly >~80%; see (*21*)]. These samples also arbitrarily contained residual Ge, as in the case of the 'HCl chemistry'. However, the 'HF chemistry' has the advantage that larger amounts of sample digests (up to ~1500 mg;

Tables S1 and S2) can be processed in a single column with 7 mL resin, in comparison to the 'HCl chemistry' [maximum ~450 mg; (*41*)].

Section S1. Se isotope systematics of marine sediments

As a redox-sensitive element, Se is commonly present in a variety of oxidation states (−2, 0, +4, and +6) in natural environments (*18, 64, 65*) (Fig. S1). Selenium occurs as 1) highly water-soluble selenate (SeO_4^{2-}) and selenite (SeO_3^{2-}) oxyanions under oxidizing conditions, and 2) insoluble Se^0 and pyrite-bound Se^{2-} as well as soluble organic Se^{2-} under reducing conditions (*18, 64, 65*) (Fig. S1). The soluble/mobile Se oxyanions only occur at relatively high redox potentials (such as oxic/suboxic conditions); therefore, the presence of free atmospheric oxygen enhances the release of reduced Se^{2-} from the continent (silicate rocks and sediments and their pyrites/sulfide minerals) via oxidative weathering and ultimately its transport to the oceans (*7, 18, 19, 65, 66*) (Fig. S1). Transitions between different oxidation states can induce strong mass-dependent isotope fractionation (up to ~19‰ in $^{82}Se/^{76}Se$ ratio), with the most significant fractionations observed during reduction reactions (SeO_4^{2-} to SeO_3^{2-} and SeO_3^{2-} to Se^0) (*18, 65*). Therefore, together with the distinct redox-dependent mobility of Se species, the Se elemental and isotopic abundances of marine sediments and pyrites can used as a proxy to constrain changes in the ocean–atmosphere redox conditions (*7, 18-20, 65, 67, 68*).

Previous studies reported considerable variability of Se isotope data for global marine sediments, with $\delta^{82}Se$ ranging between ~−3‰ and +3‰ [N = 759; (*20, 66, 68-75*)] (Fig. 1A). This mainly results from kinetic isotopic fractionation during reduction of soluble Se oxyanions (SeO_4^{2-} and SeO_3^{2-}) at various redox conditions of the water column (*18, 65*) (Fig. S1). Although modest compared to the experimental observations (see above), $\delta^{82}Se$ variations in sediments far exceed the igneous inventory range (~−0.3‰–+0.3‰; N = 87) defined by mantle-derived samples from diverse geodynamic settings [(*21, 41, 60, 61*) this work] (Fig. 1A and B). The seawater $\delta^{82}Se$ is not well constrained but probably remains slightly heavier than the igneous inventory considering the Se geochemical cycle (*65*) (Fig. S1). Selenium has a very short ocean residence time (10^4 years) and the seawater Se content is on the order of ~0.1–0.2 ng/g (*64, 65*) (Fig. 1A).

Throughout the text and figures, the mean $\delta^{82}Se$ and Se content of sediments/pyrites reported for a given geological time interval are calculated over a set of sample data that are first averaged by the same depositional age (i.e., age-averaged data; see Figs. 1, 5, and S8). This approach helps minimize overrepresentation of large numbers of sample data with the same age. The global sediment $\delta^{82}Se$ record does not show clear changes across the Great Oxidation Event [GOE; ~2.4–2.1 Ga ago; (*8*)], with essentially identical mean values of +0.57 ± 0.26‰ and +0.53 ± 0.33‰ for the Archean and Proterozoic sediments (95% CI; N = 191 and 210 individual data), respectively (Fig. 1A). However, there is a notable change in $\delta^{82}Se$ towards mostly lighter values after the Neoproterozoic oxygenation event [NOE; ~0.8–0.55 Ga ago; (*8*)], with a mean $\delta^{82}Se$

of $-0.17 \pm 0.07‰$ for the Phanerozoic sediments (95% CI; $N = 358$) (Fig. 1A). This average isotopic shift has been first suggested by Stüeken et al. (20) to reflect deep ocean oxygenation and hence widespread occurrence of Se oxyanions, hence partial reduction-induced Se isotope fractionation (e.g., during dissimilatory and diagenetic reduction) in locally suboxic/anoxic bottom water (Fig. S1). In comparison, the dominant occurrence of positive values in deep-sea sediments during the Precambrian reflects near-quantitative reduction of Se oxyanions under anoxic conditions, following partial reduction in the shallower oxic/suboxic seawater and during transport on land (65, 66) (Fig. S1).

Section S2. Selenium elemental and isotopic behavior during MORB petrogenesis

Selenium is a chalcophile element and its abundance in mantle-derived melts are dominantly controlled by the behavior of sulfide phases present during partial melting and igneous differentiation (21, 76). The igneous inventory of Se is probably dominated by its reduced form (Se^{2-}) (21, 77). Previous studies suggested that all the observed MORB glasses with near-primitive to highly evolved compositions (~9–4.5 wt. % MgO) are sulfide - saturated and thus experience continuous Se removal by sulfide segregation during their magmatic evolution (21, 46, 78, 79) (Fig. S4). Selenium abundances of the MAR basalts span a larger range (88–209 ng/g; $N = 18$) relative to the PAR basalts (158–219 ng/g; $N = 27$) (Fig. S4). Compared to the strictly co-genetic PAR samples that show strong correlation of Se with magmatic differentiation indexes such as MgO and FeO_T and other chalcophile elements such as S and Te (21), the MAR samples show little or weak correlation between Se and other indexes (Fig. S4A and B). Only the depleted MAR basalts plot close to the PAR suite with respect to both the Se–S and Se–Te variations. All these depleted MORBs from these two localities ($N = 31$), including both primitive and highly evolved samples (MgO contents 4.52–8.85 wt. %), define linear co-variation arrays with opposite respective trends (Fig. S4A and B), consistent with sulfide liquid–silicate melt partitioning of these elements in the order of Te>Se>S as previously observed [e.g., (21, 77)]. The plume-influenced MORBs show considerable scatter from the depleted MORB array (Fig. S4A and B). Because both the Se abundance and ratios of Se and other chalcophile elements in basalts are readily affected by complex magmatic processes, they are not a good tracer of mantle source compositions in the context of crustal recycling, despite the elevated Se abundance in surface materials relative to the mantle-derived samples (Fig. 1A).

The $\delta^{82}Se$ values of the MAR glasses ($N = 18$) vary from $-0.19 \pm 0.08‰$ (N-MAR depleted MORB) to $+0.14 \pm 0.08‰$ (LOMU anomaly) (Table 1), extending the $\delta^{82}Se$ range observed for the PAR depleted MORBs ($-0.30 \pm 0.08‰$–$-0.05 \pm 0.08‰$; $N = 27$) (21) towards heavier values (e.g., Fig. 3A). Systematic differences are observed between different groups of samples: $\delta^{82}Se$ of depleted MORBs from the S- and N-MAR ($-0.19 \pm 0.08‰$–$-0.06 \pm 0.08‰$; $N = 4$) and Shona anomaly MORBs ($-0.15 \pm 0.08‰$–$-0.08 \pm 0.08‰$; $N = 4$) both remain within the PAR $\delta^{82}Se$ range, whereas the majority of samples associated with the Discovery plume (i.e.,

Discovery and LOMU anomalies; $N = 10$) show heavier values (e.g., EW9309 25D-1g and 7D-1g with δ^{82}Se of $+0.09 \pm 0.08‰$ and $+0.14 \pm 0.08‰$, respectively).

Selenium isotopes do not fractionate during MORB differentiation or mantle melting involving fractionation between sulfide phases (sulfide liquid with/without monosulfide solid solution) and silicate melt, as has been previously suggested based on PAR MORB (21). The MAR samples studied here display random variations between δ^{82}Se values and MgO, FeO$_T$, and indexes of sulfide segregation such as S (642–1388 µg/g; not shown), Se (88–209 ng/g) and Se/Te ratios (14–145; Fig. S4C and D). Similar observations have been made for δ^{34}S and S abundances (15, 79). The two heaviest δ^{82}Se values ($+0.09 \pm 0.08‰$ and $+0.14 \pm 0.08‰$) characterized by the Discovery and LOMU anomaly MORBs (EW9309 25D-1g and 7D-1g) seem to be associated with the lowest S (15) and Se abundances and Se/Te ratios across the entire MAR and PAR suites (Fig. S4C and D). These MORBs represent the least differentiated samples with the two lowest FeO$_T$ contents (15), meaning that they experienced the least sulfide segregation. Should all other lighter δ^{82}Se values be caused by further sulfide segregation, one would expect to see continuous decrease of δ^{82}Se with increasing Se content or Se/Te ratio, which is not observed across a wide range of magma composition (Fig. S4C and D). We thus confirm the conclusion of ref. (21) that there is no Se isotopic fractionation during igneous processes and that MORB δ^{82}Se represents the mantle source signature. In addition, the heavy δ^{82}Se (and δ^{34}S) values were not affected by any crustal level non-magmatic processes such as assimilation of high-temperature hydrothermal fluids and associated sulfides during differentiation, because the S-MAR samples display Cl/K ratios (sensitive indicator of brine contamination) of 0.02–0.11 that fall within/close to the range of global MORB devoid of hydrothermal fluid assimilation (15, 21). Even the PAR MORBs influenced by such processes do not show noticeable change in their δ^{82}Se values (21). Finally, alteration by seawater after eruption is unlikely to modify δ^{82}Se due to the negligible Se content of seawater (see Section S1). Altogether, the observed δ^{82}Se variability of the MAR glasses must reflect source heterogeneity. The samples with the highest δ^{82}Se mentioned above also represent the two most enriched MAR basalts with respect to radiogenic isotopes, suggesting that heavy Se isotope signature of MORB is resulted from source enrichment (e.g., Fig. 3A; Fig. S5A and B).

Section S3. Selenium isotope composition of the depleted mantle

The Se isotope values of the depleted basalts from the S- and N-MAR remain within error of the PAR (depleted) basalts. Together, they yield a mean δ^{82}Se $= -0.16 \pm 0.03‰$ (95% CI, $N = 31$), which is suggested here to represent the depleted mantle Se isotopic composition (Table 1). The use of 95% CI as an uncertainty of the mean is justified by performing the Anderson-Darling normality test, which yields a test statistic of 0.39, smaller than the critical value of 0.73 at $\alpha = 0.05$ significance level. This suggests that the depleted MORB δ^{82}Se dataset can be adequately described by a normal distribution. Note that the 95% CI uncertainty of $\pm 0.03‰$ on the deplete mantle δ^{82}Se is identical to that obtained for the average of 9 replicate analyses of a single glass sample

(PAC2 DR33-1; Table S2) (*21*), which shows that the depleted mantle average δ^{82}Se value is accurate at ±0.03‰.

As for the dispersion of δ^{82}Se values within the 31 depleted MORBs, we obtain $2s = ±0.13‰$, higher than the $2s_p = ±0.08‰$ external uncertainties of our method for glass matrices (see *Main Text*, Materials and Methods). The calculated MSWD for these data is 2.60, well outside the 95% confidence interval of 0.57–1.56 given by the χ^2 statistics. These calculations imply certain isotopic variabilities detectable in the depleted MORB, which cannot be sufficiently accounted for by analytical uncertainties. We note that 2 PAR MORBs show very negative δ^{82}Se values of $-0.30 ± 0.08‰$ (*21*) (Fig. S4C and D). The Isoplot algorithm (*80*) suggests rejection of these data as statistical outlier, and for the remaining 29 samples, it yields lower reduced χ^2 of 1.80. This value still exceeds the 95% confidence interval (χ^2 statistics; see above) but is very close to the upper bound, indicating that most depleted MORBs have homogenous Se isotope composition.

The presence of small statistical δ^{82}Se variations in the depleted upper mantle might reflect intrinsic isotopic heterogeneity, commonly referred to as the marble-cake mantle model (*81*). For instance, Hamelin *et al.* (*82*) demonstrated the presence of small amounts of recycled oceanic crust components with HIMU affinity within the Pacific ambient depleted mantle that is devoid of any plume influence (Fig. 2C; Fig. S5C). Previous studies on S isotopes in global MORB also reported considerable variations in δ^{34}S for different depleted mantle domains, possibly due to varying abundance of recycled oceanic crust in the depleted mantle (*15, 46, 79*). Only two δ^{82}Se data are currently available for the altered oceanic crust and they show significantly negative values of $\sim-1.3‰$ [hydrothermally altered basalts at Menez Gwen field; (*83*)]. In this regard, presence of variable amounts of recycled oceanic crust in the PAR mantle source could in principle explain the two lightest δ^{82}Se values as well as the statistically subtle δ^{82}Se variability observed among other PAR basalts (*21*) (Fig. S4C and D) (see Section S6 for further discussion regarding the composition of altered oceanic crust). Nevertheless, the N-MAR samples, which plot among the most remarkably depleted MORBs across the global dataset with respect to all radiogenic isotopes (*51*) (Fig. 2), display identical δ^{82}Se values ($-0.17 ± 0.08‰$ and $-0.19 ± 0.08‰$; $2s_p$) to the PAR basalt average representing the Pacific depleted mantle ($-0.16 ± 0.03‰$; 95% CI, $N = 27$; Fig. 3A; Fig. S5A and B). This further attests to the robustness of the depleted mantle Se isotope composition that is calculated over all the depleted MORB data ($N = 31$).

Finally, the Se isotopic composition of the depleted mantle falls within the bulk chondrite average [$-0.21 ± 0.31‰$, $2s$; (*84*)]. The chondritic δ^{82}Se and non-chondritic δ^{34}S of the depleted mantle (*15*) reflect the contrasting timing of Se and S delivery to the present-day mantle: the mantle Se budget was established by late accretion of chondritic components (*21, 61, 85, 86*), provided that Se behaved strictly as a highly siderophile element during differentiation of the metallic core and silicate mantle [see (*21*)]; whereas the mantle S budget

was mostly established during main stage of accretion and preserves imprints of core–mantle equilibration (*15, 46, 79*).

Section S4. Coupled δ^{82}Se and δ^{34}S variations

Our data shows a correlation between δ^{82}Se and ^{87}Sr/^{86}Sr ratios ($r^2 = 0.86$, MSWD = 0.71), in a remarkably similar manner as δ^{34}S–^{87}Sr/^{86}Sr correlation [(*15*); $r^2 = 0.85$, MSWD = 5.9] (Fig. 3A and B). The δ^{82}Se and δ^{34}S values are also correlated with each other ($r^2 = 0.64$, MSWD = 1.6; Fig. 3C). All the individual δ^{82}Se ($N = 45$) and δ^{34}S ($N = 51$) data across the entire MAR and PAR MORB suites [(*15, 21, 46*); this work] show highly consistent distribution patterns (Fig. 3C; Fig. S6F). For both isotope systematics, the Discovery and LOMU anomalies (both genetically linked to the Discovery mantle plume; Methods) extend the depleted MORB mantle range towards heavier values, with the Shona anomaly in between (Fig. 3; Fig. S6). The difference in the average δ^{82}Se between the depleted MORBs and Shona anomalies are not statistically significant (Student's *t*-test, two-tailed *p*-value 0.41), whereas the difference between the depleted MORBs and Discovery + LOMU anomalies are statistically significant (*p*-value 0.02). For the latter comparison, if all the depleted MORBs from the MAR and PAR are considered, the *p*-value becomes extremely small (~0.00001).

The coupled δ^{82}Se–δ^{34}S variations in different groups of S-MAR basalts are further illustrated for other geochemical tracers of mantle source enrichment, such as ^{143}Nd/^{144}Nd (Fig. S6) and key incompatible trace/major element ratios [Ba/Nb, (La/Sm)$_N$, and K_2O/TiO_2; Fig. S7]. Isotopic enrichment observed in the same group of basalts can be decoupled from specific element ratios to different extents, depending on the effect of melting processes on elemental fractionation (*44, 57*). For example, EW9309 25D-1g, the most radiogenic (^{87}Sr/^{86}Sr = 0.705728) sample in our dataset, shows only moderately elevated (La/Sm)$_N$ relative to depleted MORBs (*57*). Still, systematic covariations are apparent between the average δ^{82}Se–δ^{34}S values and presented elemental ratios across different groups of basalts, in a similar manner shown for radiogenic isotopes (Figs. S6 and S7). These observations and similar elemental/isotopic behavior of Se–S during mantle processes (*15, 21, 46, 79*), despite the large differences in redox potential required for Se^{2-}–SeO_4^{2-} and S^{2-}–SO_4^{2-} transitions in surface aqueous environments [e.g., (*18, 65, 67*)], argue for an overall similar behavior of these chalcophile stable isotope systems during crustal recycling.

Section S5. Details of the mixing model

Previous studies suggested that the pronounced radiogenic isotope variabilities observed in the S-MAR basalts (Fig. 2) require presence of a variety of enriched recycled components (such as ancient oceanic crust, sediment, delaminated subcontinental lithospheric mantle, and lower continental crust) in the Discovery and Shona plumes, which locally influence the S-MAR depleted mantle (*22-24*). However, Labidi *et al.* (*15*) argued that the S isotope systematics mainly reflect sediment recycling based on the observed linear S–radiogenic isotope

covariation trends (e.g., Fig. 3B), which requires the enriched end-member to be sufficiently rich in S. Pelagic sediments deposited during the Proterozoic with an average model recycling age of ~1.5 Ga would satisfy both radiogenic and S (δ^{34}S and mass-independent) isotope systematics of the plume-influenced S-MAR basalts (*15, 22, 24*). Considering the similar geochemical behavior of Se and S isotope systems as discussed above, one might expect that the Se isotope variability beneath the S-MAR also dominantly reflects sediment recycling as in the case of S isotopes (*15*). Furthermore, the linear correlation between the isotope compositions of the lithophile element Sr and chalcophile elements Se and S within the MORB data range (Fig. 3A and B) implies that the sulfide phases (major hosts of Se and S) and other silicate matrices might be efficiently homogenized *locally* in the compositionally heterogeneous (*22*) Shona and Discovery mantle plumes. This could be achieved if the sulfide phases were molten within the plume at certain conditions in the convective upper mantle (*21, 26*).

Variations of δ^{82}Se–^{87}Sr/^{86}Sr and δ^{82}Se–δ^{34}S in the studied MORBs (Figs. 3 and 4) can be indeed explained by a binary mixing between the depleted mantle and enriched component that is demonstrated here to be sediments. First, our compiled sediment data yield a mean δ^{82}Se = +0.62 ± 0.50‰ (1*s*, *N* = 76) for sediments formed during 1–2 Ga, which would readily account for the positive slope of the trend. Extrapolations of the error-weighted linear regressions [2*s* external uncertainty on each isotope composition of samples or end-members is considered; Isoplot (*80*)] to a 1.5 Ga old recycled pelagic sediment model composition of ^{87}Sr/^{86}Sr ≈ 0.7203 and δ^{34}S ≈ +10‰ (*15, 27*) yield δ^{82}Se of +1.44 ± 0.39‰ and +1.15 ± 0.41‰, respectively (95% CI). If we relax the age constraints for the sediment end-member by using a range of other broadly possible recycling ages [e.g., ~1–2 Ga (*15*)], the linear mixing curve in Fig. 4B would result in slightly different δ^{82}Se for recycled sediments. For instance, 1 and 2 Ga old pelagic sediments have ^{87}Sr/^{86}Sr ratios of 0.7175 and 0.7236 [calculated following the isotopic evolution model of Rehkämper and Hofmann (*27*); see Table S3], which yield δ^{82}Se of +1.19 ± 0.33‰ and +1.74 ± 0.47‰, respectively (95% CI). Again, both values are within uncertainty typical of mid-Proterozoic sediments (Fig. 5A). As discussed in the main text, all of our model results for δ^{82}Se of the sediment end-member at a range of possible mid-Proterozoic recycling ages (1–2 Ga) (Fig. 4A) remain realistic for abyssal pelagic sediments subducted from a redox-stratified ocean.

Next, the simple linear mixing arrays shown in Figs. 3 and 4 require the same Se–S–Sr elemental ratios within uncertainties for both the depleted mantle and enriched end-members. If we take 0.080 ± 0.017 µg/g Se, 9.80 ± 1.86 µg/g Sr, and 200 ± 40 µg/g S for the depleted mantle (*21, 86-88*), and 300 ± 17 µg/g Sr (assigned error from GLOSS-II) and 5700 ± 1000 µg/g S for the 1.5 Ga old recycled pelagic sediment (*15, 27, 89*), the calculated Se contents of the sediment end-member are 2.45 ± 0.71 and 2.28 ± 0.78 µg/g (at depleted mantle Se/Sr = 0.0082 ± 0.0023 and Se/S = 0.00040 ± 0.00012), respectively (uncertainties are all 1*s*; see Table S3 for model parameters and results). Using the mean δ^{82}Se and Se content of the sediment end-member obtained from the δ^{82}Se–^{87}Sr/^{86}Sr and δ^{82}Se–δ^{34}S mixing relationships (Fig. 3A and C), we successfully reproduce the

covariation between $\delta^{82}Se$ and $^{143}Nd/^{144}Nd$ (Fig. S5A). It shows a parabolic rather than linear mixing trend due to the higher Nd/Se ratios of sediments (~36) relative to the depleted mantle (Table S3). Noting that S content of sediment end-member from (*15*) is itself defined by S–radiogenic isotope mixing relationships, we use Se content as well as $\delta^{82}Se$ of recycled sediment inferred from the $\delta^{82}Se$–$^{87}Sr/^{86}Sr$ variation (Figs. 3A and 4) for our discussion in the following and main text.

The calculated Se content of recycled sediment (2.45 ± 0.71 μg/g) falls close to the upper bound of observed sediment average, which is essentially the same for the 1–2 Ga interval ($0.85^{+2.12}_{-0.61}$ μg/g; 1*s*, *N* = 76) or entire Proterozoic ($0.56^{+2.27}_{-0.45}$ μg/g; 1*s*, *N* = 218) (Table S3 and Fig. 4B). This is consistent with insignificant, if there is any, Se loss from the bulk sedimentary slab material and hence associated isotopic fractionation during subduction zone processing in the mid-Proterozoic and large-scale recycling within the mantle. This is reminiscent of the case of S systematics, further highlighting similarity between Se and S isotopic/elemental behavior during recycling (*15, 21*) (see Section S4). We note that this might be different after the Neoproterozoic Oxygenation Event (NOE) when a fully oxygenated bottom ocean may have had consequences on the redox budget of slab-derived components at subduction zones [e.g., (*13, 17, 20*)]. Another line of evidence for insignificant Se modification during sediment subduction comes from Se systematics of arc-related magmas: 1) Se contents of the most primitive (>~8 wt. % MgO) subduction zone magmas (e.g., glasses from the Mariana arc, Eastern Manus Back-arc Basin, and Southern-Valu Fa Ridge) are comparable to or lower than that of primitive MORB at a given MgO; 2) $\delta^{82}Se$ values observed for Mariana arc lavas (~−0.33‰–+0.03‰), although indicating addition of heavy sedimentary Se isotopes at this *modern* subduction zone, are within the global MORB range (~−0.30‰–+0.14‰; Fig. 1B) [(*21, 60, 78*); this work]; both ranges of $\delta^{82}Se$ values are quite limited relative to the observed (Fig. 1A) or calculated (e.g., Fig. 5A) range of marine sediments. These observations point to limited Se addition from the bulk subducting sediment to the sub-arc mantle wedge and associated Se isotope fractionation at the slab scale. Furthermore, previous studies pointed out that S elemental/isotopic signature of sediments (more specifically, reduced S in sedimentary sulfides) experienced insignificant or only moderate modification during subduction processing—sediment dehydration releasing S_2-bearing fluids and melting [(*15, 90*); and references therein]. The following comparisons between Se and S isotope and elemental behavior in low- and high-temperature systems leads to important inferences that recycled sediments (especially from the anoxic deep ocean in mid-Proterozoic) are even more unlikely to experience any significant Se loss during subduction, leading to efficient Se recycling into the mantle: 1) fluid-mobile, oxidized species of Se occurs at much higher redox potential compared to that of S in low-temperature environments (*18, 65*); 2) there is limited Se isotope fractionation during oxidation in low-temperature environments (Fig. S1); 3) Se is more chalcophile than S and thus more compatible (in terms of sediment residue/melt) during magmatic processes (*21, 76*); 4) Se isotopes are not fractionated during magmatic processes [(*21*) and this work].

All the arguments presented above suggest that the Se systematics of the recycled sediment would resemble that of the subducting protolith at the surface. We calculate the Se content of sedimentary pyrite using the Se content of recycled sediment (2.45 ± 0.71 µg/g; $1s$), assuming that Se-bearing pyrite in marine sediments is of $FeSe_xS_{(2-x)}$ composition (x is extremely small). First, a compilation of S_{pyrite} (mass fraction of S as pyrite) in 1– 2 Ga old global sediments (*10, 29*) gives an average of $1.1^{+1.4}_{-0.6}$ wt. % (log-normal mean; $1s$, $N = 85$), corresponding to $2.1^{+2.6}_{-1.1}$ wt. % pyrite in the bulk sediment. In the next step, 1) if Se budget of the bulk sediment is fully contributed by pyrite, we obtain pyrite Se content of 119^{+155}_{-74} µg/g (propagated $1s$; Fig. 5C); 2) if Se is hosted by both pyrite and other matrices (organic matter, clay, and other silicates), given the mean pyrite/matrix Se ratio of ~5.82 observed in global marine black shales (*19*), we obtain pyrite Se content of 13^{+4}_{-4} µg/g (propagated $1s$; Fig. 5C). These two values, on average, represent the upper and lower bound of our estimate in a linear mixing model (Fig. 5C). A more realistic value probably tends towards our 'lower estimate' due to the appreciable fraction of organic-bound Se in the mid-Proterozoic compared to Phanerozoic (*20*), and this 'lower estimate' is remarkably comparable within error to the observed pyrite averages for the 1–2 Ga interval (19^{+33}_{-12} µg/g) or entire Proterozoic [16^{+24}_{-10} µg/g, $1s$; (*7, 19, 28*)] (Fig. 5C and Fig. S8E).

In order to explore if alternative non-linear mixing models also lead to the same conclusion, we calculate possible Se contents of the sediment end-member at fixed $\delta^{82}Se$ values of $1s$ and $2s$ above the observed mean of 1–2 Ga old sediments (green and blue mixing curves in Fig. 4B or Fig. S8B). These $\delta^{82}Se$ represent the upper bound values in the statistical sense with respect to the individual ($N = 76$) or age-averaged ($N = 9$) sediment $\delta^{82}Se$ data for the 1–2 Ga interval (Fig. S8C and the histogram) that is relevant for our discussion, and would result in the minimum possible range of sediment Se contents. This is calculated by error-weighted least-squares fitting of the mixing hyperbola to the MORB data (using OriginPro software; OriginLab, Northampton, MA), where $\delta^{82}Se$, $^{87}Sr/^{86}Sr$, Se/Sr of depleted mantle and $^{87}Sr/^{86}Sr$, Sr content of sediment end-member are well-constrained parameters, and the curvature of the hyperbola is defined by $R = (Se/Sr)_{sediment}/(Se/Sr)_{mantle}$ (Fig. 4B or Fig. S8B; see Table S3 for model parameters). We obtain the best-fit R values of 1.34 ± 0.19 and 0.92 ± 0.12 (95% CI) at $\delta^{82}Se$ of $1s$ and $2s$ above the sediment mean, respectively (Fig. 4B or Fig. S8B). The goodness-of-fit of the model is evaluated by MSWD statistics (incorporating external uncertainties on both $\delta^{82}Se$ and $^{87}Sr/^{86}Sr$): the best-fit R values correspond to the lowest MSWD at a degree of freedom of 18, that is the number of data points ($N = 19$) minus the number of model parameters to be calculated (1 in this case). Selenium contents of the recycled sediment and sedimentary pyrite are then calculated accordingly (the quoted errors in the text and Table S3 are always propagated in the calculation) (Fig. S8D and E). All these alternative hyperbolic mixing models yield a 'lower estimate' of recycled pyrite Se content (i.e., if Se in the bulk sediment is hosted by both pyrite and other matrices; see above) that is comparable within error to the observed average of the 1–2 Ga old sedimentary pyrites (19^{+33}_{-12} µg/g, $1s$; Fig. S8E).

Section S6. Role of other recycled components

First, we consider the possibility of delaminated subcontinental lithospheric mantle and lower continental crust (EM1 and LOMU components; Fig. 2) (*22-24*) as carriers of the heave Se isotope signatures in the Discovery plume-influenced S-MAR basalts. Worldwide peridotites derived from the subcontinental lithospheric mantle have comparable Se contents (mean $0.054^{+0.076}_{-0.032}$ μg/g; 1*s*, *N* = 11) to the depleted mantle and display a narrow δ^{82}Se range with a mean of −0.03 ± 0.02‰ [95% CI, *N* = 11; (*61*)] (Fig. 1B). They thus cannot explain the observed ^{82}Se-enrichments by mixing with the depleted mantle (e.g., Fig. 3A). As for the lower continental crust, estimated Se content varies from ~0.05 to 0.2 μg/g in the literature [e.g., (*91*)]. These values might be potentially lower compared to the Se content of the delaminated lower crust due to the pervasive deep-seated cumulate-hosted sulfides that are enriched in strongly chalcophile elements such as Se (*92*). There is no literature Se isotope data for continental crust materials. Based on the δ^{82}Se values of the Proterozoic Västervik granitoids (~0.20‰; Table S2) and other mantle-derived samples, it is very likely that the Se isotopic composition of the lower continental crust does not significantly deviate from the igneous inventory range (~−0.3‰–+0.3‰; Fig. 1B). Therefore, despite the potentially higher Se content relative to the depleted mantle, the delaminated lower continental crust cannot explain the observed δ^{82}Se–^{87}Sr/^{86}Sr trend defined by the MORB samples (Fig. 3A).

We do not observe clear correlation between δ^{82}Se and ^{206}Pb/^{204}Pb ratios (Fig. S5C). Three Shona anomaly basalts carrying clear HIMU-like signatures with the highest ^{206}Pb/^{204}Pb and mildly elevated ^{87}Sr/^{86}Sr (Fig. 2C) show identical δ^{82}Se values to the depleted mantle composition (Fig. S5C). As mentioned previously, two δ^{82}Se data published so far for the altered oceanic crust show significantly negative values of ~−1.3‰, with anomalously enriched Se contents of ~60 μg/g (*83*). The altered oceanic crust could potentially experience Se loss during subduction due to slab dehydration (hence associated sulfide loss), which is assumed to be the same extent as S and Pb loss [58–98%; (*46*)]. This, according to the data of Rouxel *et al.* (*83*), allows estimation of Se content in the recycled oceanic crust at ~1–25 μg/g. A HIMU plume component with this high Se content and light δ^{82}Se value would readily result in lighter δ^{82}Se with increasing ^{206}Pb/^{204}Pb in the S-MAR basalts, which is not observed (Fig. S5C). Also, it cannot explain the observed δ^{82}Se–δ^{34}S variation (Fig. 3C) due to the much lower S/Se ratios in the HIMU end-member (~16) relative to the depleted mantle (~2500), which would generate a concave-upward mixing hyperbola that lies outside the observed data range [assuming δ^{34}S = 3‰ and ~18–385 μg/g S for HIMU, following (*46*)]. Importantly, we note that the altered oceanic basalts studied by Rouxel *et al.* (*83*) represent exceptionally Se-enriched proportion of the oceanic crust due to their proximity to the hydrothermal field, and unlikely reflect the composition of the bulk/global altered oceanic crust. Future studies are necessary to further constrain the Se systematics of the HIMU end-member.
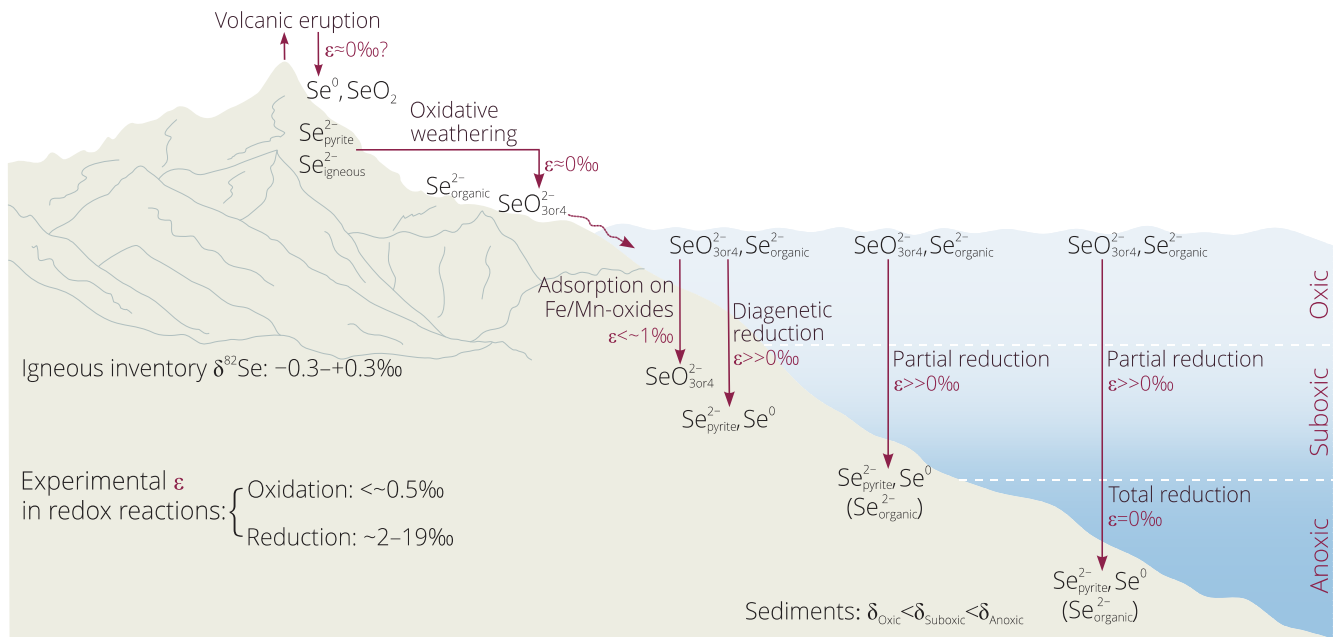
Fig. S1. Selenium cycle in marine environment. It shows the major processes controlling the transport and fate of Se on the continental crust and in a redox-stratified open ocean (not to scale; modified after Stüeken *et al.* (*66*). The mid-Proterozoic marine redox conditions might have been mostly euxinic in continental margin/slope settings and ferruginous in the deep ocean (*9*). The crustal δ^{82}Se is represented by the igneous inventory range compiled in this work (see Fig. 1B). The experimental isotope fractionation ε ($\varepsilon = \delta^{82}Se_{reactant} - \delta^{82}Se_{product}$) in low-temperature redox reactions (SeO$_4^{2-}$ to SeO$_3^{2-}$ and SeO$_3^{2-}$ to Se^0) is from compilation of ref. (*18*); ε during Se adsorption onto Fe and Mn oxides is small [$\varepsilon < \sim 0.5$–0.8‰; (*93*)]. The sense of isotopic fractionation during subaerial volcanic activity between the silicate magma Se$_{igneous}^{2-}$ and volcanic gas species Se^0 and/or SeO$_2$ [both readily depositing on surface upon cooling; (*94*)] remains unknown, but the magnitude of ε might be significantly small compared to the low-temperature aqueous experiments, as inferred from the *relatively* limited difference in δ^{82}Se between submarine MORB glasses and worldwide subaerial lavas (Fig. 1B).
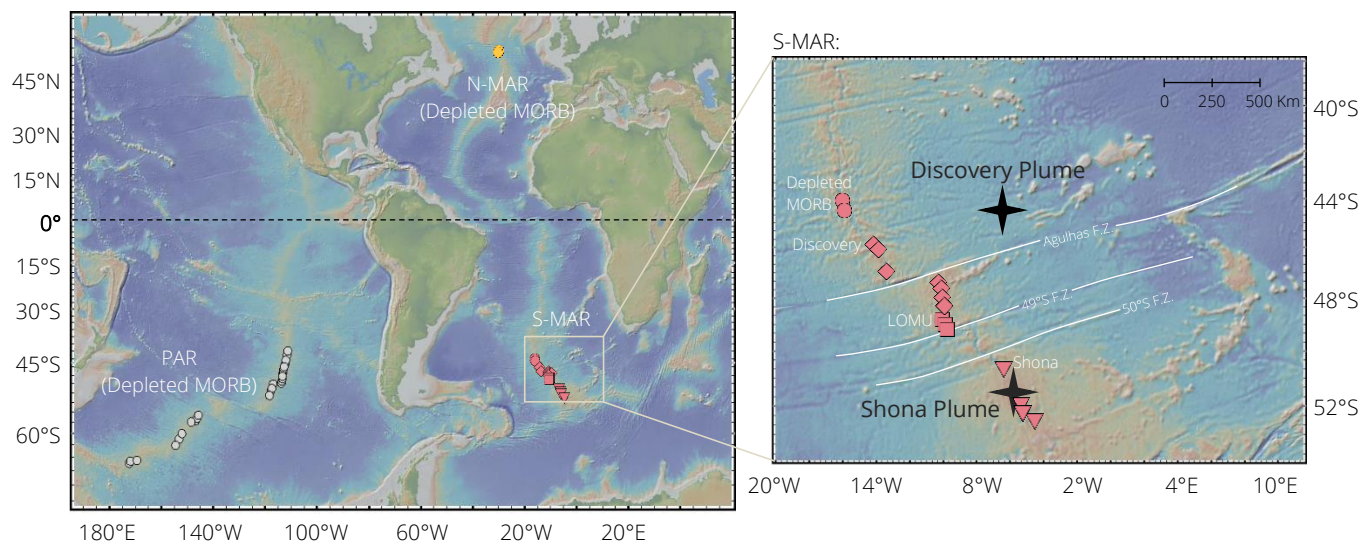
Fig. S2. Sample locations along the N- and S-MAR. Location of the PAR MORB suite is shown for comparison ($N = 27$). Also shown in detail are the locations of the off-ridge Discovery plume and ridge-centered Shona plume, as well as the principle first-order tectonic discontinues (fracture zones; F.Z.) across the studied S-MAR sections. Samples associated with different plume contributions are displayed with different symbols. The regional map is generated by the GeoMapApp (http://www.geomapapp.org).
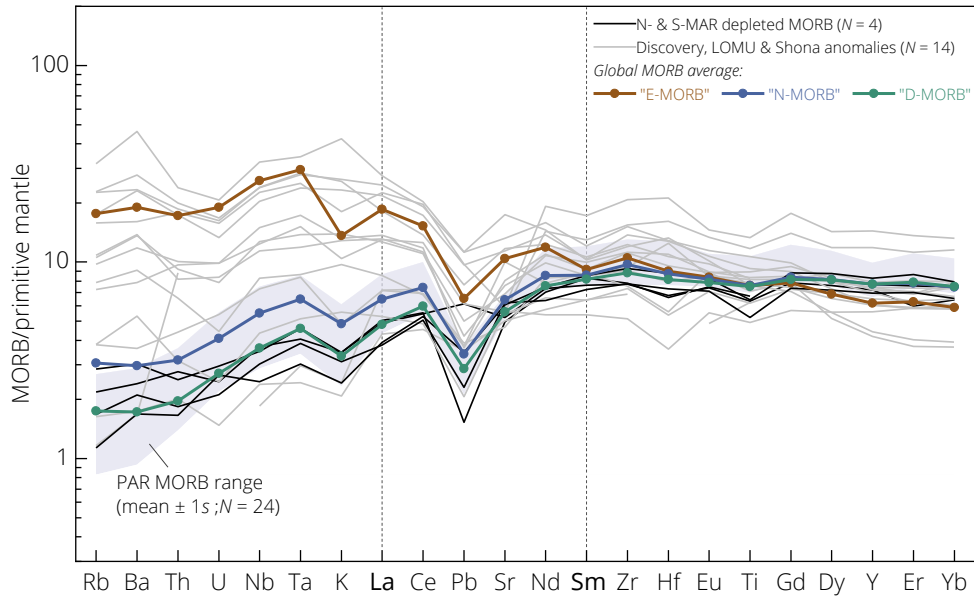
Fig. S3. Primitive mantle-normalized trace element patterns. Normalizing values are from (*85*). Samples are plotted as two separate groups: the depleted MORBs (black solid lines; (La/Sm)$_N$ 0.457–0.643) and MORBs associated with mantle plume enrichment (grey solid lines; (La/Sm)$_N$ 0.670–2.681, mostly >1). Shown for comparison are the PAR MORB range (shaded area; average ± 1s) (*21*) and global MORB averages (*95*).
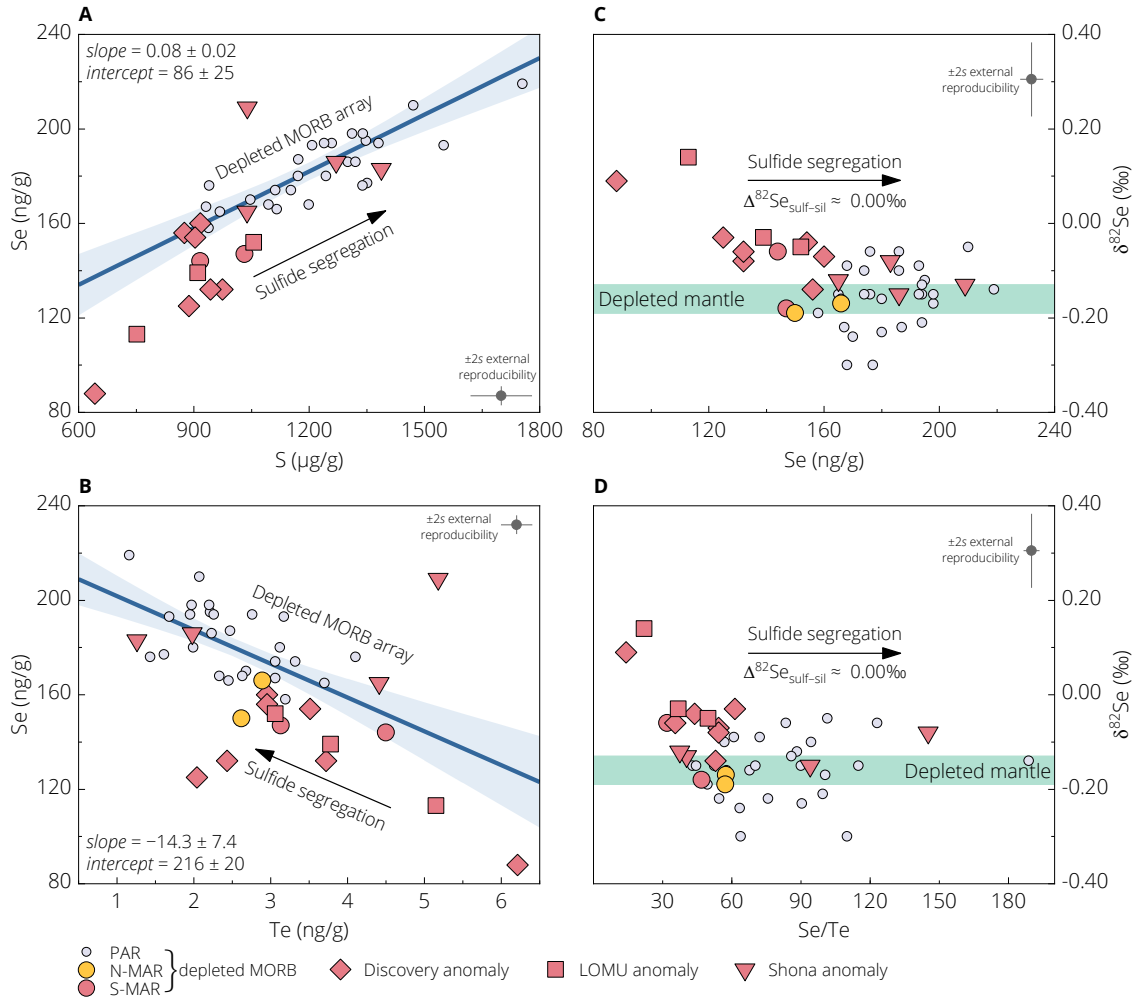
Fig. S4. Selenium vs. chalcophile elements S and Te, and δ^{82}Se vs. Se abundances and Se/Te ratios. Shown for comparison are the published data for PAR MORB (*21*). The error bars represent the typical ±2*s* external reproducibilities for S, Se, and Te contents and pooled ±2s_p external reproducibility for δ^{82}Se [(*21, 46*); Table S2]. (**A, B**) All depleted MORBs from the MAR and PAR ranging from primitive and highly evolved basalts (MgO 4.52–8.85 wt. %) display linear Se–S and Se–Te co-variation arrays with opposite trends as indicated by the regression line (shaded areas are 95% CI envelope; errors on the slope and intercept are 95% CI). (**C, D**) Depleted mantle δ^{82}Se from Table 1. Δ^{82}Se$_{sulf–sil}$: Se isotope fractionation between sulfides and silicate melt.
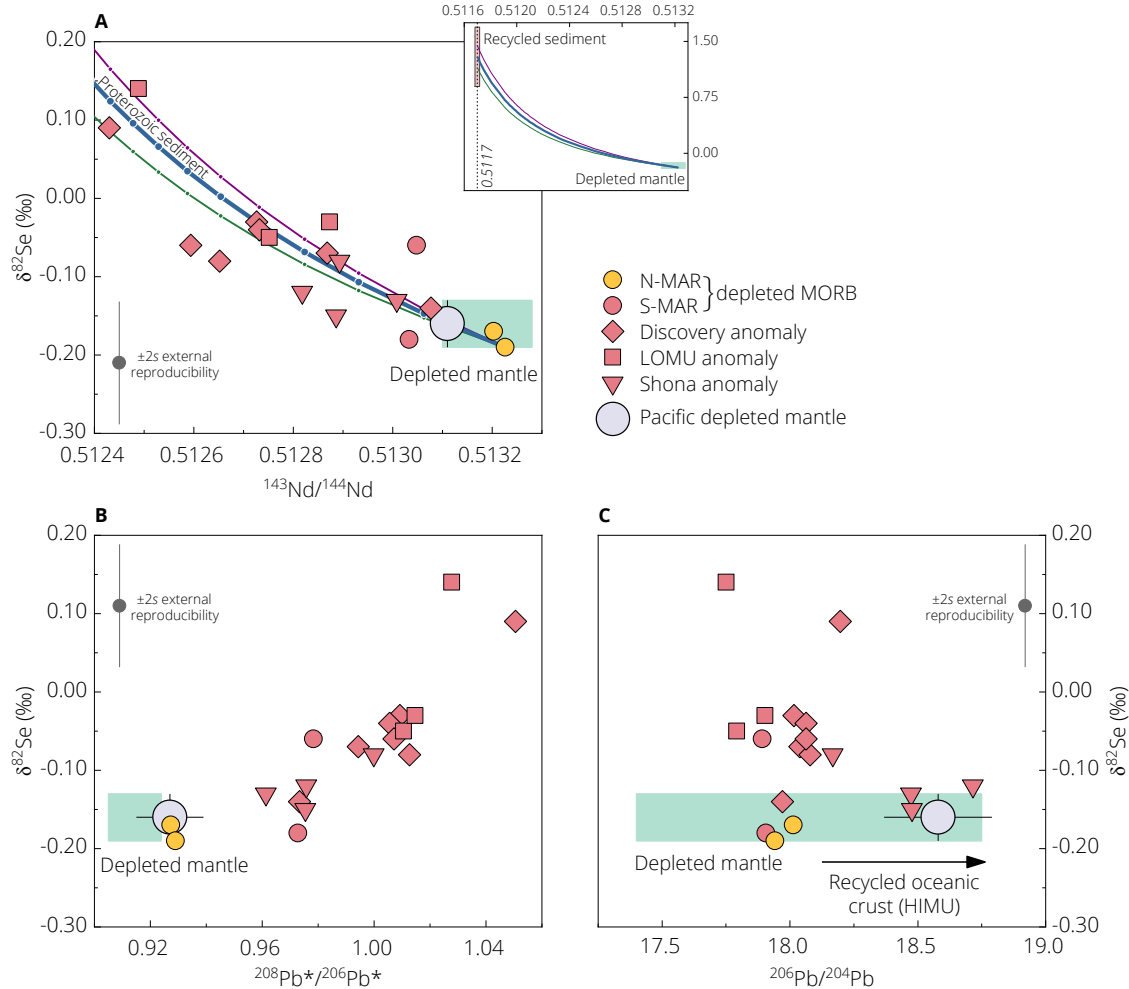
Fig. S5. δ⁸²Se vs. ¹⁴³Nd/¹⁴⁴Nd, ²⁰⁸Pb*/²⁰⁶Pb*, and ²⁰⁶Pb/²⁰⁴Pb. It shows that Se isotopes are correlated with ¹⁴³Nd/¹⁴⁴Nd (**A**) and ²⁰⁸Pb*/²⁰⁶Pb* (**B**), but not with ²⁰⁶Pb/²⁰⁴Pb (**C**). ²⁰⁸Pb*/²⁰⁶Pb* = (²⁰⁸Pb/²⁰⁴Pb − 29.476)/(²⁰⁶Pb/²⁰⁴Pb − 9.307) is the time-integrated Th/U ratio (*44*). (**A**) The mixing trends accounting for the Se–Nd isotopic variation are calculated using the most depleted S-MAR basalt (TR138 08D-1g) as an anchor and the best-fit parameters (Se content and δ⁸²Se) for the sediment end-member obtained from the δ⁸²Se – ⁸⁷Sr/⁸⁶Sr (purple line) and δ⁸²Se–δ³⁴S (green line) linear relationships (see Fig. 3). Average of these best-fit parameters is used to generate the mixing curve shown in thick blue line. See also (**A**) inset for the 1.5 Ga old recycled sediment composition (pink box, mean δ⁸²Se ± 95% CI). Each tick mark on the mixing curve (**A**) indicates 0.1 wt. % sediment addition to the depleted mantle (as in Fig. 3). Depleted mantle Nd content (0.713 μg/g) from (*88*); Nd and Se isotopic compositions of the depleted mantle and Pacific ambient depleted mantle from Table 1; 1.5 Ga old pelagic sediment Nd content (85 μg/g) and ¹⁴³Nd/¹⁴⁴Nd (0.5117) from (*27*). See Table S3 for the full list of mixing parameters.
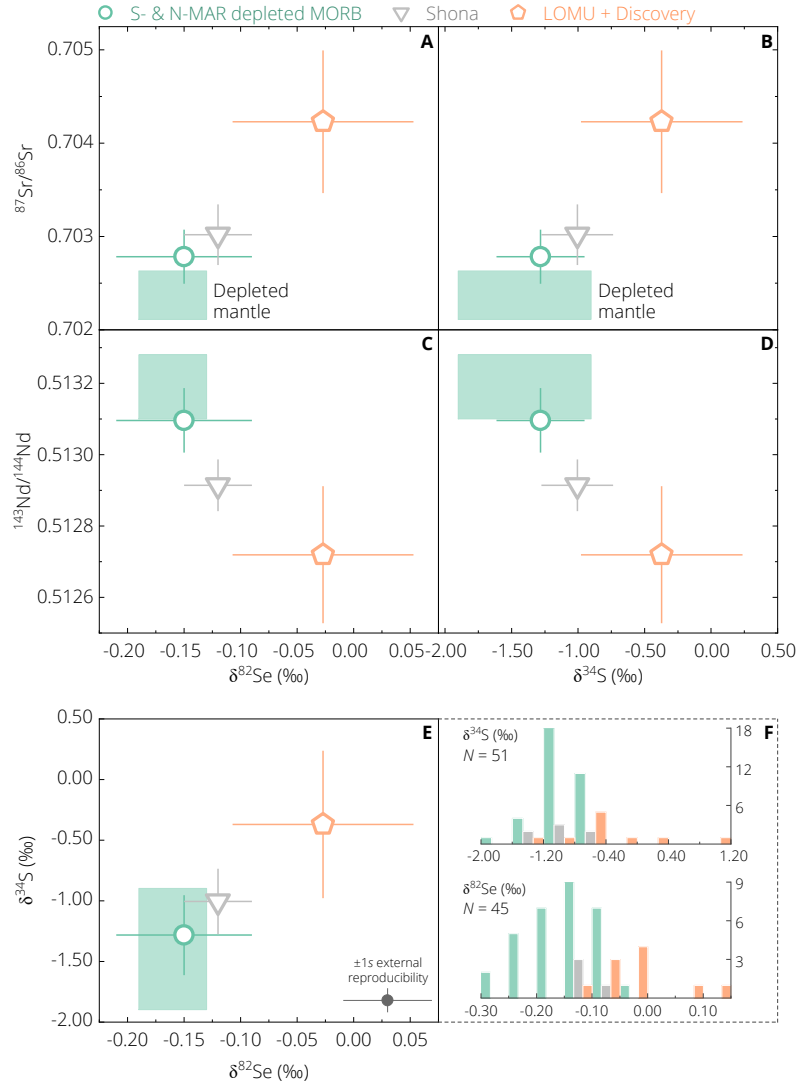
Fig. S6. Average Se, S, Sr, and Nd isotope compositions of the three groups of MAR basalts. (**A–D**) δ^{82}Se and δ^{34}S vs ^{87}Sr/^{86}Sr and ^{143}Nd/^{144}Nd. E, δ^{82}Se vs δ^{34}S, with (**F**) displaying the frequency histogram for the entire dataset of the MAR and PAR MORBs [bin width 0.05‰ for δ^{82}Se and 0.4‰ for δ^{34}S; (*15, 21, 46*) and this work). Additional S, Sr, and Nd isotope data for the S-MAR (*15*) are also included in the calculation of the group means (uncertainties are ±1*s* for all isotopes). Depleted mantle composition from Table 1.
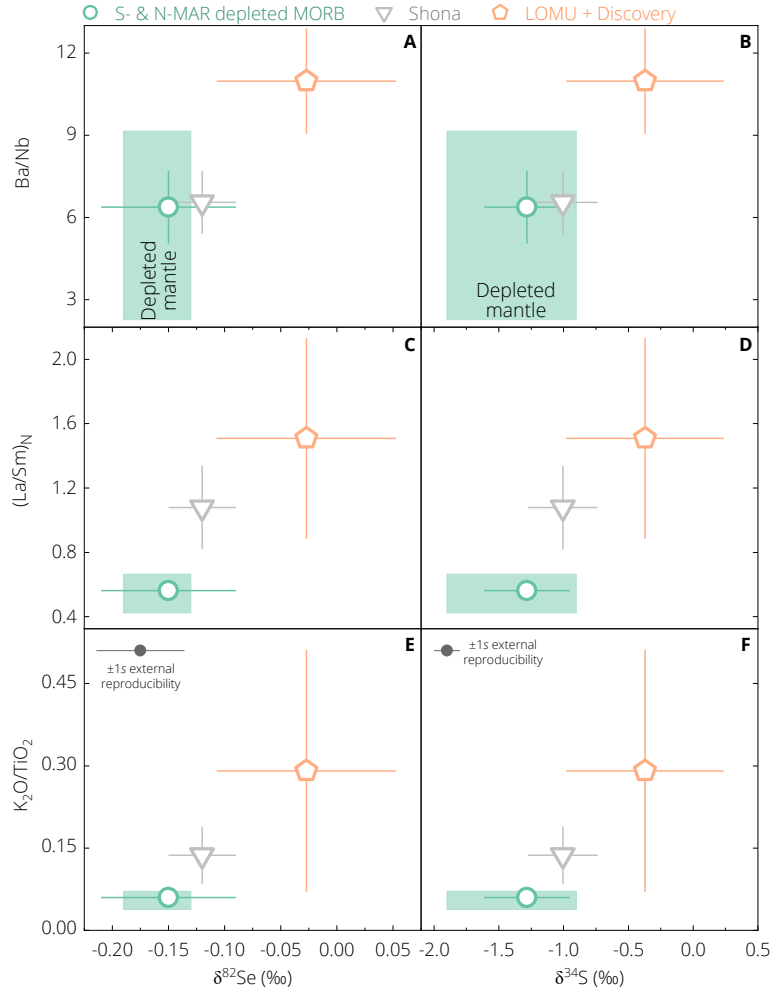
Fig. S7. Average δ⁸²Se and δ³⁴S of the three groups of MAR glasses plotted against key trace/major element ratios. Additional δ³⁴S and concentration data for the S-MAR (*15, 46*) are also included in the calculation of the group means (uncertainties are ±1*s*). Composition of the depleted mantle, trace/major elements from (*88*) and δ⁸²Se and δ³⁴S from Table 1.
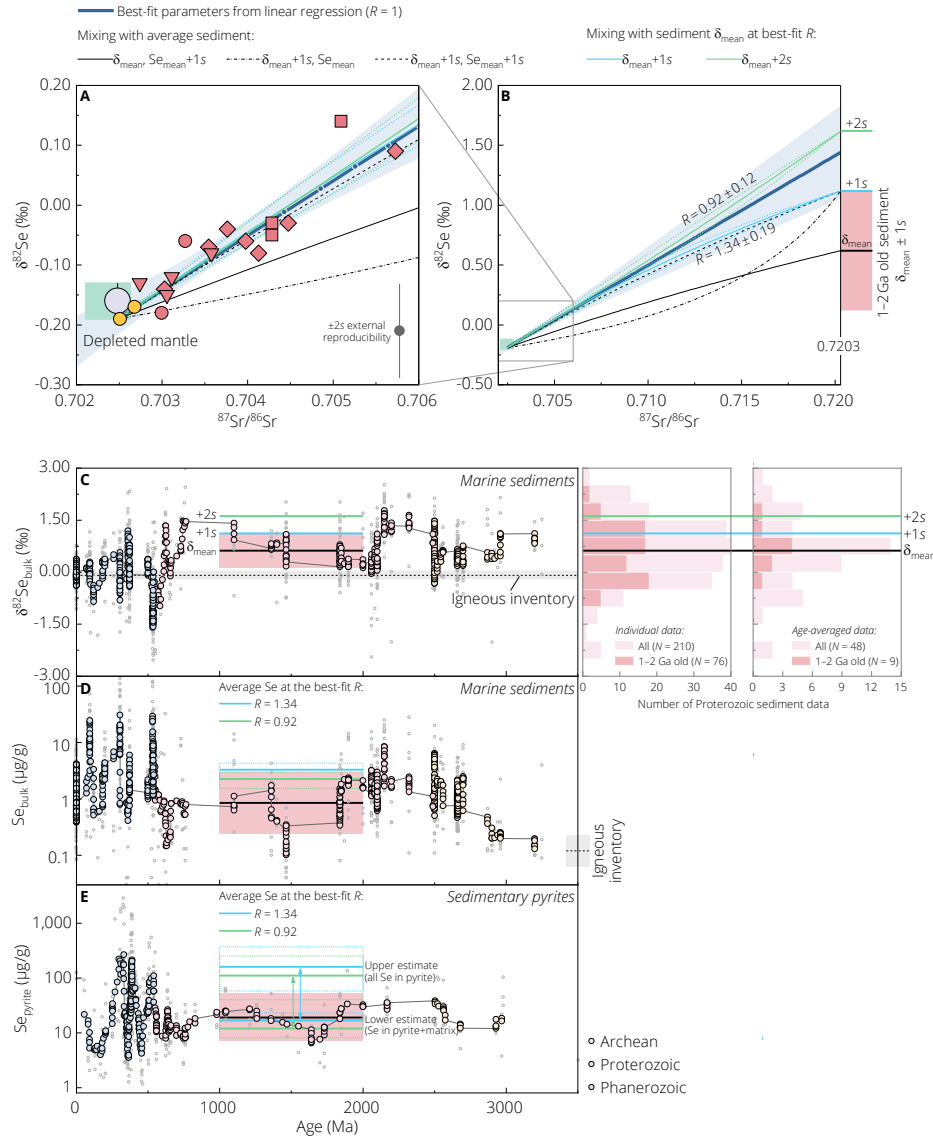
Fig. S8. Mixing models with parameters from 1–2 Ga old pelagic sediments and results. (**A**, **B**) are the same figure as Fig. 4. $R = (Se/Sr)_{sediment}/(Se/Sr)_{mantle}$. (**C–E**) Literature data are presented in the same manner as in Fig. 5A–C, with the thick black line and shaded field indicating the observed mean ± 1s of 1–2 Ga old marine sediments. Right panels of **C**: shown for comparison are the frequency histogram of individual and age-averaged sediment δ^{82}Se data for the entire Proterozoic Eon and 1–2 Ga interval that is relevant for our discussion. (**D**, **E**) show our modeling results for ~1.5 Ga old recycled sediment/pyrite (color-coded boxes: mean = thick solid line; 1s error = short-dashed line) corresponding to the model input in (**A**, **B**), i.e., δ^{82}Se values of 1s (blue line) and 2s (green line) above the sediment average (black line). All errors on the model parameters (see Table S3) are propagated when calculating Se contents of recycled sediment/pyrite. See Section S5 for more details.

Table S1. Selenium isotope and elemental abundances of international rock standards analyzed in this work and literature data.

Rock standard/Type	Location	Individual measurement				Mean						
		Sample weight (mg)	δ^{82}Se (‰)	Internal error[‡]	Se (ng/g)	δ^{82}Se (‰)	2s	95% CI	n	Se (ng/g)	2s	n
BHVO-2, USGS (*ocean island basalt*)	Hawaii, USA	399.96	0.20	0.03	170	0.14	0.10		4	171	7	4
		319.14[*]	0.11	0.04	165							
		422.70[*]	0.18	0.04	171							
		353.88[*,†]	0.13	0.06	174							
		353.88[*,†]	0.08	0.06	174							
Yierpan *et al.* (*21*)						0.10	0.11		4	165	4	4
Yierpan *et al.* (*41*)						0.18	0.10		8	169	6	61
Varas-Reus *et al.* (*61*)						0.15	0.10		4	170	8	4
Grand mean						**0.15**	**0.11**	**0.03**	**20**	**169**	**7**	**73**
BCR-2, USGS (*continental flood basalt*)	Columbia River, USA	1019.16[*]	0.27	0.05	78					78	3	1
Yierpan *et al.* (*21*)						0.17	0.11		2	79	3	2
Yierpan *et al.* (*41*)						0.29	0.10		5	76	2	18
Kurzawa *et al.* (*42*)						0.18	0.11		3	71	8	3
Lissner *et al.* (*76*)										78	6	5
Grand mean						**0.23**	**0.13**	**0.04**	**11**	**76**	**3**	**24**
BE-N, CRPG (*continental basalt*)	near Essey-la-côte, France											
Yierpan *et al.* (*41*)						**0.15**	**0.10**	**0.06**	**5**	**66**	**2**	**23**
Rouxel *et al.* (*83*)						0.37	0.32		1	57		1
Lissner *et al.* (*76*)										65	1	3
BIR-1a, USGS (*Icelandic basalt*)	near Reykjavik, Iceland	1529.38[*]	0.33	0.06	15					15	1	1
Yierpan *et al.* (*41*)						0.28	0.11		5	15	1	5
Grand mean						**0.29**	**0.10**	**0.05**	**6**	**15**	**1**	**6**
JB-2, GSJ (*basalt*)	Oshima, Japan											
Kurzawa *et al.* (*60*)						**-0.19**	**0.12**		**3**	**153**	**10**	**6**

Rock standard/Type	Location	Individual measurement				Mean						
		Sample weight (mg)	δ^{82}Se (‰)	Internal error‡	Se (ng/g)	δ^{82}Se (‰)	2s	95% CI	n	Se (ng/g)	2s	n
JB-3, GSJ (*basalt*)	Narusawa-mura, Japan											
Kurzawa *et al.* (*60*)						**0.16**	**0.12**		**2**	**67**	**4**	**2**
JGb-1, GSJ (*gabbro*)	Funehiji-machi, Japan	401.92†	-0.23	0.07	178	**-0.25**	**0.12**		**1**	**178**	**7**	**1**
		401.92†	-0.27	0.09	178							
MRG-1, CCRMP (*gabbro*)	Montreal, Canada	211.68†	0.08	0.06	214	**0.09**	**0.12**		**1**	**214**	**9**	**1**
		211.68†	0.10	0.07	214							
JA-3, GSJ (*andesite*)	Tsumagoi-mura, Japan	625.57	0.26	0.06	58	**0.26**	**0.12**		**1**	**58**	**2**	**1**
W-2a, USGS (*diabase*)	near Centreville, USA	401.76	-0.01	0.06	106	-0.05	0.10		2	106	4	2
		273.05	-0.08	0.05	106							
Yierpan *et al.* (*21, 41*)						-0.07	0.12		7	107	2	9
Grand mean						**-0.07**	**0.11**	**0.04**	**9**	**107**	**4**	**11**

Recommended values for rock standards (highlighted in bold) are calculated using all the data obtained under intermediate precision conditions (i.e., at Uni. Tübingen); 2s uncertainties on δ^{82}Se are directly calculated if the total number of digestions $n>3$, or estimated with the $2s_p$ external reproducibility of 0.12‰ (estimated for non-glass matrices; see Materials and Methods) if $n\leq3$; 2s on Se abundances are 4% two relative standard deviation (*41*). δ^{82}Se data of ref. (*83*) is converted relative to NIST SRM 3149 standard [see (*21*)].

*Sample digests processed through the 'HF chemistry'; all other sample digests were processed through the 'HCl chemistry' following Yierpan *et al.* (*41*).

†Different aliquots of a sample digest.

‡Internal error is 95% CI over 40 cycles of integration in each individual measurement.

Table S2. Selenium isotope and/or Se–Te elemental analyses of MORBs, granitoids, and the inter-laboratory standard solution MH-495.

Sample	Note	Individual measurement					Mean		
		Sample weight (mg)	δ^{82}Se (‰)	Internal error	Se (ng/g)	Te (ng/g)	δ^{82}Se (‰)	Uncertainty	Se (ng/g)
	Southern Mid-Atlantic ridge								
EW9309 41D-1g		308.28	-0.03	0.04	144	4.50	-0.06	0.08	144
		208.77	-0.08	0.08	145				
EW9309 40D-1g		315.88*	-0.23	0.05	146	3.13	-0.18	0.08	147
		316.42†	-0.17	0.10	147				
		316.42†	-0.15	0.05	147				
EW9309 34D-1g		302.36	-0.07	0.04	161	2.95	-0.07	0.08	160
EW9309 33D 1g		326.75	-0.06	0.04	126	2.04	-0.03	0.08	125
		249.38	0.01	0.06	125				
EW9309 28D-1g		315.52	-0.16	0.09	156	2.95	-0.14	0.08	156
		323.08*	-0.12	0.06	156				
EW9309 25D-1g		366.37	0.05	0.06	89	6.21	0.09	0.08	88
		349.07	0.16	0.11	88				
		279.17	0.08	0.08	89				
		282.61*	0.08	0.06	88				
EW9309 2D-1g		300.29	-0.10	0.06	132	2.43	-0.08	0.04	132
		275.94†	-0.05	0.06	132				
		275.94†	-0.08	0.07	132				
		215.94	-0.10	0.07	133				
EW9309 4D-3g		323.71	-0.04	0.04	153	3.51	-0.04	0.08	154
		312.54*	-0.03	0.07	153				
EW9309 5D 5g		327.89	-0.03	0.04	132	3.72	-0.06	0.08	132
		294.06*	-0.09	0.10	133				

Sample	Note	Individual measurement					Mean		
		Sample weight (mg)	$\delta^{82}Se$ (‰)	Internal error	Se (ng/g)	Te (ng/g)	$\delta^{82}Se$ (‰)	Uncertainty	Se (ng/g)
EW9309 7D-1g		326.18	0.09	0.05	112	5.15	0.14	0.08	113
		196.85	0.15	0.07	114				
		406.76*	0.18	0.09	113				
EW9309 8D-1g		320.42	-0.03	0.05	152	3.06	-0.05	0.08	152
		188.21	-0.04	0.07	152				
		299.23*	-0.08	0.03	153				
EW9309 9D-3g		257.39	-0.03	0.04	140	3.78	-0.03	0.04	139
		239.61	-0.04	0.04	139				
		244.32	-0.07	0.05	142				
		262.65	-0.01	0.04	136				
		260.52	0.03	0.06	137				
		356.77*	-0.04	0.04	139				
EW9309 15D-1g		339.95	-0.12	0.03	213	5.18	-0.13	0.08	209
		319.97*	-0.14	0.04	209				
EW9309 21D-1g		329.60	-0.11	0.04	165	4.41	-0.12	0.08	165
		309.97*	-0.13	0.06	165				
EW9309 23D-1g		303.32	-0.19	0.05	188	1.98	-0.15	0.08	186
		302.05*	-0.10	0.07	188				
EW9309 22D-3g		307.20†	-0.10	0.05	183	1.26	-0.08	0.08	183
		307.20†	-0.06	0.05	183				
	Northern Mid-Atlantic ridge								
TR138 09D-2g		403.57	-0.17	0.03	162	2.89	-0.17	0.08	166
TR138 08D-1g		401.88	-0.20	0.04	150	2.62	-0.19	0.08	150
		252.63	-0.18	0.05	150				

Sample	Note	Individual measurement					Mean		
		Sample weight (mg)	$\delta^{82}Se$ (‰)	Internal error	Se (ng/g)	Te (ng/g)	$\delta^{82}Se$ (‰)	Uncertainty	Se (ng/g)
	Pacific-Antarctic ridge								
PAC2 DR33-1[‡]		150	-0.16	0.03	201	2.14	-0.15	0.03	199
		210[†]	-0.10	0.04	198	2.20			
		210[†]	-0.11	0.07	198				
		232	-0.16	0.03	198	2.18			
		238	-0.19	0.04	198				
		241	-0.18	0.03	197	2.23			
		255	-0.22	0.03	199	2.27			
		402[†]	-0.12	0.04	201	2.17			
		402[†]	-0.10	0.05	201				
	Västervik granitoids								
SES 3-05	Quartzmonzonite–Monzogranite	1498.53[*]	0.24	0.05	21.2		0.24	0.12	21.2
SES 19-05	Quartzmonzonite–Monzogranite	1003.71[*]	0.19	0.05	35.4		0.19	0.12	35.4
SES 1-96	Monzogranite	1213.43[*]	0.18	0.07	28.3		0.18	0.12	28.3

MH-495 (30 ng/mL Se)		**Long-term analytical reproducibility[§]**
	This work	-3.25 ± 0.07‰ (2*s*; *n* = 53)
	Yierpan *et al.* (*41*)	-3.26 ± 0.06‰ (2*s*; *n* = 32)
	Yierpan *et al.* (*21*)	-3.24 ± 0.07‰ (2*s*; *n* = 20)
	Kurzawa *et al.* (*60*)	-3.25 ± 0.08‰ (2*s*; *n* = 26)
	Varas-Reus *et al.* (*61*)	-3.25 ± 0.08‰ (2*s*; *n* = 69)
	Grand mean	**-3.25 ± 0.07‰ (2*s*; *n* = 200)**

Uncertainties on the mean $\delta^{82}Se$ are 95% CI if the number of analyses $n_i>3$, or the $2s_p$ external reproducibility of 0.08‰ (estimated for glass matrices) if $n_i \leqslant 3$; 2*s* on Se (one isotope dilution data is also included when calculating the mean) and Te concentrations are ~3–5% two relative standard deviation [external reproducibility for glass matrices; this work and (*21*)].

[*]Sample digests processed through the 'HF chemistry'; all other sample digests were processed through the 'HCl chemistry' following (*41*).

[†]Different aliquots of a sample digest.

[‡]Data from (*21*).

[§]The 2*s* analytical reproducibility of our method is evaluated from 200 measurements of MH-495 under intermediate precision conditions over the course of 24 months.

Table S3. Parameters and results from the two-component mixing model and compositions of marine sediments/pyrites.

	δ^{82}Se (‰)	Se (μg/g)	^{87}Sr/^{86}Sr	Sr (μg/g)	^{143}Nd/^{144}Nd	Nd (μg/g)	δ^{34}S (‰)	S (μg/g)
End-members								
Depleted mantle	−0.16 ± 0.03 or *−0.19 ± 0.08*	0.080 ± 0.017	0.70248 ± 0.00003	9.80 ± 1.86	*0.513226 ± 0.000006*	0.713 ± 0.050	−1.4 ± 0.5	200 ± 40
1.5 Ga old recycled pelagic sediment	1.44 ± 0.39 (+1.15 ± 0.41)*	2.45 ± 0.71 (2.28 ± 0.78)*	0.7203†	300 ± 17‡	0.5117	85	+10 ± 3	5700 ± 1000
1.5 Ga old recycled sedimentary pyrite§		13^{+4}_{-4} and 119^{+155}_{-74}						
Marine sediments								
Archean	0.57 ± 0.45 (*M* = 14, *N* = 191)	$0.59^{+1.09}_{-0.38}$ (*M* = 14, *N* = 193)						
Proterozoic	0.53 ± 1.13 (*M* = 48, *N* = 210)	$0.56^{+2.27}_{-0.45}$ (*M* = 55, *N* = 218)						
1–2 Ga time interval	0.62 ± 0.50 (*M* = 9, *N* = 76)	$0.85^{+2.12}_{-0.61}$ (*M* = 9, *N* = 76)						
Phanerozoic	−0.17 ± 0.44 (*M* = 142, *N* = 358)	$1.00^{+2.98}_{-0.75}$ (*M* = 147, *N* = 364)						
Marine pyrites								
Archean		21^{+38}_{-14} (*M* = 11, *N* = 25)						
Proterozoic		16^{+24}_{-10} (*M* = 49, *N* = 113)						
1–2 Ga time interval		19^{+33}_{-12} (*M* = 17, *N* = 38)						
Phanerozoic		22^{+113}_{-18} (*M* = 90, *N* = 209)						

The mixing trends are generated using compositions of the Pacific depleted mantle or the most depleted MORB TR138 08D-1g as indicated by italics (see Figs. 3A and 4 and Fig. S5A). Uncertainties on mixing end-member elemental concentrations (*15, 21, 27, 86-88*) and on Se contents/δ^{82}Se values of marine sediments/pyrites (*7, 19, 20, 28, 66, 68-75*) are all 1*s*. Uncertainties on mixing end-member isotope compositions are as reported in Table 1 and literature [1*s* on ^{143}Nd/^{144}Nd of the sample TR138 08D-1g (*52*) and 1*s* on δ^{34}S of the recycled sediment (*15*)]. *M* = number of age-averaged data, *N* = number of different sediment/pyrite samples from the literature.

*The best-fit parameters from the linear regression through the δ^{82}Se–δ^{34}S data. Noting that S content of sediment end-member from (15) is itself defined by S–radiogenic isotope mixing relationships, we use Se content as well as δ^{82}Se of recycled sediment inferred from the δ^{82}Se–^{87}Sr/^{86}Sr variation (Figs. 3A and 4) for our discussion.

†Taken from (27). The present-day ^{87}Sr/^{86}Sr ratios of pelagic sediments at other broadly possible recycling ages T (between 1 and 2 Ga; e.g., see Fig. 5A) are calculated according to the isotopic evolution model of (27): from 4.55 Ga to T, ^{87}Rb/^{86}Sr = 0.186; from T to present day, ^{87}Rb/^{86}Sr = 0.61. All other parameters used to construct the present-day ^{87}Sr/^{86}Sr of pelagic sediments (such as the age, ^{87}Sr/^{86}Sr, and ^{87}Rb/^{86}Sr of the Bulk Earth and decay constant of ^{87}Rb) are in accordance with (96).

‡Assigned error from GLOSS-II (89) as there was no uncertainty considered for pelagic sediment Sr content in (27). Note that both types of sediment end-members have identical Sr contents (but not Nd).

§Upper and lower bound of our estimated Se content in recycled pyrite (see Section S5 for further details).

REFERENCES AND NOTES

1. I. H. Campbell, C. M. Allen, Formation of supercontinents linked to increases in atmospheric oxygen. *Nat. Geosci.* **1**, 554–558 (2008).

2. C. B. Keller, B. Schoene, Statistical geochemistry reveals disruption in secular lithospheric evolution about 2.5 Gyr ago. *Nature* **485**, 490–493 (2012).

3. L. R. Kump, M. E. Barley, Increased subaerial volcanism and the rise of atmospheric oxygen 2.5 billion years ago. *Nature* **448**, 1033–1036 (2007).

4. C.-T. A. Lee, L. Y. Yeung, N. R. McKenzie, Y. Yokoyama, K. Ozaki, A. Lenardic, Two-step rise of atmospheric oxygen linked to the growth of continents. *Nat. Geosci.* **9**, 417–424 (2016).

5. M. A. Smit, K. Mezger, Earth's early O_2 cycle suppressed by primitive continents. *Nat. Geosci.* **10**, 788–792 (2017).

6. H. D. Holland, The oxygenation of the atmosphere and oceans. *Philos. Trans. R. Soc. Lond. B Biol. Sci.* **361**, 903–915 (2006).

7. R. R. Large, I. Mukherjee, D. Gregory, J. Steadman, R. Corkrey, L. V. Danyushevsky, Atmosphere oxygen cycling through the Proterozoic and Phanerozoic. *Miner. Deposita* **54**, 485–506 (2019).

8. T. W. Lyons, C. T. Reinhard, N. J. Planavsky, The rise of oxygen in Earth's early ocean and atmosphere. *Nature* **506**, 307–315 (2014).

9. S. W. Poulton, D. E. Canfield, Ferruginous conditions: A dominant feature of the ocean through Earth's history. *Elements* **7**, 107–112 (2011).

10. C. Scott, T. W. Lyons, A. Bekker, Y. Shen, S. W. Poulton, X. Chu, A. D. Anbar, Tracing the stepwise oxygenation of the Proterozoic ocean. *Nature* **452**, 456–459 (2008).

11. E. A. Sperling, C. J. Wolock, A. S. Morgan, B. C. Gill, M. Kunzmann, G. P. Halverson, F. A. Macdonald, A. H. Knoll, D. T. Johnston, Statistical analysis of iron geochemical data suggests limited late Proterozoic oxygenation. *Nature* **523**, 451–454 (2015).

12. P. J. Patchett, W. M. White, H. Feldmann, S. Kielinczuk, A. W. Hofmann, Hafnium/rare earth element fractionation in the sedimentary system and crustal recycling into the Earth's mantle. *Earth Planet. Sci. Lett.* **69**, 365–378 (1984).

13. M. B. Andersen, T. Elliott, H. Freymuth, K. W. Sims, Y. Niu, K. A. Kelley, The terrestrial uranium isotope cycle. *Nature* **517**, 356–359 (2015).

14. R. A. Cabral, M. G. Jackson, E. F. Rose-Koga, K. T. Koga, M. J. Whitehouse, M. A. Antonelli, J. Farquhar, J. M. Day, E. H. Hauri, Anomalous sulphur isotopes in plume lavas reveal deep mantle storage of Archaean crust. *Nature* **496**, 490–493 (2013).

15. J. Labidi, P. Cartigny, M. Moreira, Non-chondritic sulphur isotope composition of the terrestrial mantle. *Nature* **501**, 208–211 (2013).

16. H. Liu, R. E. Zartman, T. R. Ireland, W. D. Sun, Global atmospheric oxygen variations recorded by Th/U systematics of igneous rocks. *Proc. Natl. Acad. Sci. U.S.A.* **116**, 18854–18859 (2019).

17. D. A. Stolper, C. E. Bucholz, Neoproterozoic to early Phanerozoic rise in island arc redox state due to deep ocean oxygenation and increased marine sulfate levels. *PNAS* **116**, 8746–8755 (2019).

18. T. M. Johnson, T. D. Bullen, Mass-dependent fractionation of selenium and chromium isotopes in low-temperature environments. *Rev. Mineral. Geochem.* **55**, 289–317 (2004).

19. R. R. Large, J. A. Halpin, L. V. Danyushevsky, V. V. Maslennikov, S. W. Bull, J. A. Long, D. D. Gregory, E. Lounejeva, T. W. Lyons, P. J. Sack, P. J. McGoldrick, C. R. Calver, Trace element content of sedimentary pyrite as a new proxy for deep-time ocean–atmosphere evolution. *Earth Planet. Sci. Lett.* **389**, 209–220 (2014).

20. E. E. Stüeken, R. Buick, A. Bekker, D. Catling, J. Foriel, B. M. Guy, L. C. Kah, H. G. Machel, I. P. Montanez, S. W. Poulton, The evolution of the global selenium cycle: Secular trends in Se isotopes and abundances. *Geochim. Cosmochim. Acta* **162**, 109–125 (2015).

21. A. Yierpan, S. König, J. Labidi, R. Schoenberg, Selenium isotope and S-Se-Te elemental systematics along the Pacific-Antarctic ridge: Role of mantle processes. *Geochim. Cosmochim. Acta* **249**, 199–224 (2019).

22. M. Andres, J. Blichert-Toft, J.-G. Schilling, Hafnium isotopes in basalts from the southern Mid-Atlantic Ridge from 40°S to 55°S: Discovery and Shona plume-ridge interactions and the role of recycled sediments. *Geochem. Geophys. Geosyst.* **3**, 1–25 (2002).

23. J. Douglass, J.-G. Schilling, D. Fontignie, Plume-ridge interactions of the Discovery and Shona mantle plumes with the southern Mid-Atlantic Ridge (40°-55°S). *J. Geophys. Res.* **104**, 2941–2962 (1999).

24. P. J. le Roux, A. P. le Roex, J.-G. Schilling, N. Shimizu, W. W. Perkins, N. J. G. Pearce, Mantle heterogeneity beneath the southern Mid-Atlantic Ridge: Trace element evidence for contamination of ambient asthenospheric mantle. *Earth Planet. Sci. Lett.* **203**, 479–498 (2002).

25. E. M. Syracuse, G. A. Abers, Global compilation of variations in slab depth beneath arc volcanoes and implications. *Geochem. Geophys. Geosyst.* **7**, 10.1029/2005GC001045 (2006).

26. Z. Zhang, A. von der Handt, M. M. Hirschmann, An experimental study of Fe–Ni exchange between sulfide melt and olivine at upper mantle conditions: Implications for mantle sulfide compositions and phase equilibria. *Contrib. Mineral. Petrol.* **173**, 19 (2018).

27. M. Rehkämper, A. W. Hofmann, Recycled ocean crust and sediment in Indian Ocean MORB. *Earth Planet. Sci. Lett.* **147**, 93–106 (1997).

28. I. Mukherjee, R. R. Large, R. Corkrey, L. V. Danyushevsky, The Boring Billion, a slingshot for complex life on Earth. *Sci. Rep.* **8**, 4432 (2018).

29. S. W. Poulton, P. W. Fralick, D. E. Canfield, The transition to a sulphidic ocean approximately 1.84 billion years ago. *Nature* **431**, 173–177 (2004).

30. E. J. Bellefroid, A. V. S. Hood, P. F. Hoffman, M. D. Thomas, C. T. Reinhard, N. J. Planavsky, Constraints on Paleoproterozoic atmospheric oxygen levels. *Proc. Natl. Acad. Sci. U.S.A.* **115**, 8104–8109 (2018).

31. D. E. Canfield, S. Zhang, A. B. Frank, X. Wang, H. Wang, J. Su, Y. Ye, R. Frei, Highly fractionated chromium isotopes in Mesoproterozoic-aged shales and atmospheric oxygen. *Nat. Commun.* **9**, 2871 (2018).

32. G. J. Gilleaudeau, R. Frei, A. J. Kaufman, L. C. Kah, K. Azmy, J. K. Bartley, P. Chernyavskiy, A. H. Knoll, Oxygenation of the mid-Proterozoic atmosphere: Clues from chromium isotopes in carbonates. *Geochem Perspect Let* **2**, 178–187 (2016).

33. N. J. Planavsky, C. T. Reinhard, X. Wang, D. Thomson, P. McGoldrick, R. H. Rainbird, T. Johnson, W. W. Fischer, T. W. Lyons, Earth history. Low mid-Proterozoic atmospheric oxygen levels and the delayed rise of animals. *Science* **346**, 635–638 (2014).

34. S. Zhang, X. Wang, H. Wang, C. J. Bjerrum, E. U. Hammarlund, M. M. Costa, J. N. Connelly, B. Zhang, J. Su, D. E. Canfield, Sufficient oxygen for animal respiration 1,400 million years ago. *Proc. Natl. Acad. Sci. U.S.A.* **113**, 1731–1736 (2016).

35. L. J. Alcott, B. J. W. Mills, S. W. Poulton, Stepwise Earth oxygenation is an inherent property of global biogeochemical cycling. *Science* **366**, 1333–1337 (2019).

36. M. D. Brasier, J. F. Lindsay, A billion years of environmental stability and the emergence of eukaryotes: New data from northern Australia. *Geology* **26**, 555–558 (1998).

37. P. A. Cawood, C. J. Hawkesworth, Earth's middle age. *Geology* **42**, 503–506 (2014).

38. C. Doglioni, J. Pignatti, M. Coleman, Why did life develop on the surface of the Earth in the Cambrian? *Geosci. Front.* **7**, 865–873 (2016).

39. W. B. Hamilton, Toward a myth-free geodynamic history of Earth and its neighbors. *Earth Sci. Rev.* **198**, 102905 (2019).

40. I. Mukherjee, R. R. Large, Co-evolution of trace elements and life in Precambrian oceans: The pyrite edition. *Geology*, (2020).

41. A. Yierpan, S. König, J. Labidi, T. Kurzawa, M. G. Babechuk, R. Schoenberg, Chemical sample processing for combined selenium isotope and selenium-tellurium elemental investigation of the Earth's igneous reservoirs. *Geochem. Geophys. Geosyst.* **19**, 516–533 (2018).

42. T. Kurzawa, S. König, J. Labidi, A. Yierpan, R. Schoenberg, A method for Se isotope analysis of low ng-level geological samples via double spike and hydride generation MC-ICP-MS. *Chem. Geol.* **466**, 219–228 (2017).

43. R. C. Hin, C. D. Coath, P. J. Carter, F. Nimmo, Y. J. Lai, P. A. E. Pogge von Strandmann, M. Willbold, Z. M. Leinhardt, M. J. Walter, T. Elliott, Magnesium isotope evidence that accretional vapour loss shapes planetary compositions. *Nature* **549**, 511–515 (2017).

44. A. Stracke, Earth's heterogeneous mantle: A product of convection-driven interaction between crust and mantle. *Chem. Geol.* **330-331**, 274–299 (2012).

45. A. Agranier, J. Blichert-Toft, D. Graham, V. Debaille, P. Schiano, F. Albarede, The spectra of isotopic heterogeneities along the mid-Atlantic Ridge. *Earth Planet. Sci. Lett.* **238**, 96–109 (2005).

46. J. Labidi, P. Cartigny, C. Hamelin, M. Moreira, L. Dosso, Sulfur isotope budget (^{32}S, ^{33}S, ^{34}S and ^{36}S) in Pacific–Antarctic ridge basalts: A record of mantle source heterogeneity and hydrothermal sulfide assimilation. *Geochim. Cosmochim. Acta* **133**, 47–67 (2014).

47. D. I. Groves, R. M. Vielreicher, R. J. Goldfarb, K. C. Condie, Controls on the heterogeneous distribution of mineral deposits through time. *Geol Soc Spec Publ* **248**, 71–101 (2005).

48. J.-I. Kimura, J. B. Gill, P. E. van Keken, H. Kawabata, S. Skora, Origin of geochemical mantle components: Role of spreading ridges and thermal evolution of mantle. *Geochem. Geophys. Geosyst.* **18**, 697–734 (2017).

49. J. Douglass, J.-G. Schilling, R. H. Kingsley, Influence of the discovery and Shona mantle plumes on the southern Mid-Atlantic ridge: Rare earth evidence. *Geophys. Res. Lett.* **22**, 2893–2896 (1995).

50. J.-G. Schilling, M. Zajac, R. Evans, T. Johnston, W. White, J. D. Devine, R. Kingsley, Petrologic and geochemical variations along the Mid-Atlantic ridge from 29 degrees N to 73 degrees N. *Am. J. Sci.* **283**, 510–586 (1983).

51. W. M. White, J.-G. Schilling, The nature and origin of geochemical variation in Mid-Atlantic Ridge basalts from the Central North Atlantic. *Geochim. Cosmochim. Acta* **42**, 1501–1516 (1978).

52. J. Blichert-Toft, A. Agranier, M. Andres, R. Kingsley, J.-G. Schilling, F. Albarède, Geochemical segmentation of the Mid-Atlantic Ridge north of Iceland and ridge-hot spot interaction in the North Atlantic. *Geochem. Geophys. Geosyst.* **6**, (2005).

53. M. Moreira, T. Staudacher, P. Sarda, J.-G. Schilling, C. J. Allègre, A primitive plume neon component in MORB: The Shona ridge-anomaly, South Atlantic (51–52°S). *Earth Planet. Sci. Lett.* **133**, 367–377 (1995).

54. P. Sarda, M. Moreira, T. Staudacher, J.-G. Schilling, C. J. Allègre, Rare gas systematics on the southernmost Mid-Atlantic Ridge: Constraints on the lower mantle and the Dupal source. *J. Geophys. Res.* **105**, 5973–5996 (2000).

55. K. A. Kelley, R. Kingsley, J.-G. Schilling, Composition of plume-influenced mid-ocean ridge lavas and glasses from the Mid-Atlantic Ridge, East Pacific Rise, Galápagos Spreading Center, and Gulf of Aden. *Geochem. Geophys. Geosyst.* **14**, 223–242 (2013).

56. P. J. le Roux, A. le Roex, J.-G. Schilling, Crystallization processes beneath the southern Mid-Atlantic Ridge (40–55°S), evidence for high-pressure initiation of crystallization. *Contrib. Mineral. Petrol.* **142**, 582–602 (2002).

57. P. J. le Roux, A. le Roex, J.-G. Schilling, MORB melting processes beneath the southern Mid-Atlantic Ridge (40–55°S): A role for mantle plume-derived pyroxenite. *Contrib. Mineral. Petrol.* **144**, 206–229 (2002b).

58. I. C. Kleinhanns, M. J. Whitehouse, N. Nolte, W. Baero, F. Wilsky, B. T. Hansen, R. Schoenberg, Mode and timing of granitoid magmatism in the Västervik area (SE Sweden, Baltic Shield): Sr–Nd isotope and SIMS U–Pb age constraints. *Lithos* **212-215**, 321–337 (2015).

59. N. Nolte, I. C. Kleinhanns, W. Baero, B. T. Hansen, Petrography and whole-rock geochemical characteristics of Västervik granitoids to syenitoids, southeast Sweden: Constraints on petrogenesis and tectonic setting at the southern margin of the Svecofennian domain. *Gff* **133**, 173–196 (2011).

60. T. Kurzawa, S. König, J. C. Alt, A. Yierpan, R. Schoenberg, The role of subduction recycling on the selenium isotope signature of the mantle: Constraints from Mariana arc lavas. *Chem. Geol.* **513**, 239–249 (2019).

61. M. I. Varas-Reus, S. König, A. Yierpan, J. P. Lorand, R. Schoenberg, Selenium isotopes as tracers of a late volatile contribution to Earth from the outer Solar System. *Nat. Geosci.* **12**, 779–782 (2019).

62. O. Rouxel, A. Galy, H. Elderfield, Germanium isotopic variations in igneous rocks and marine sediments. *Geochim. Cosmochim. Acta* **70**, 3387–3400 (2006).

63. T. Yokoyama, A. Makishima, E. Nakamura, Evaluation of the coprecipitation of incompatible trace elements with fluoride during silicate rock dissolution by acid digestion. *Chem. Geol.* **157**, 175–187 (1999).

64. G. A. Cutter, L. S. Cutter, Sources and cycling of selenium in the western and equatorial Atlantic Ocean. *Deep-Sea Res. Pt Ii* **48**, 2917–2931 (2001).

65. E. E. Stüeken, Selenium isotopes as a biogeochemical proxy in deep time. *Rev. Mineral. Geochem.* **82**, 657–682 (2017).

66. E. E. Stüeken, R. Buick, A. D. Anbar, Selenium isotopes support free O2 in the latest Archean. *Geology* **43**, 259–262 (2015).

67. S. König, B. Eickmann, T. Zack, A. Yierpan, M. Wille, H. Taubald, R. Schoenberg, Redox induced sulfur-selenium isotope decoupling recorded in pyrite. *Geochim. Cosmochim. Acta* **244**, 24–39 (2019).

68. K. Mitchell, P. R. D. Mason, P. Van Cappellen, T. M. Johnson, B. C. Gill, J. D. Owens, J. Diaz, E. D. Ingall, G. J. Reichart, T. W. Lyons, Selenium as paleo-oceanographic proxy: A first assessment. *Geochim. Cosmochim. Acta* **89**, 302–317 (2012).

69. M. A. Kipp, T. J. Algeo, E. E. Stüeken, R. Buick, Basinal hydrographic and redox controls on selenium enrichment and isotopic composition in Paleozoic black shales. *Geochim. Cosmochim. Acta*, (2019).

70. M. A. Kipp, E. E. Stueken, A. Bekker, R. Buick, Selenium isotopes record extensive marine suboxia during the Great Oxidation Event. *Proc. Natl. Acad. Sci. U.S.A.* **114**, 875–880 (2017).

71. M. C. Koehler, R. Buick, M. A. Kipp, E. E. Stueken, J. Zaloumis, Transient surface ocean oxygenation recorded in the ~2.66-Ga Jeerinah Formation, Australia. *Proc. Natl. Acad. Sci. U.S.A.* **115**, 7711–7716 (2018).

72. K. Mitchell, S. Z. Mansoor, P. R. D. Mason, T. M. Johnson, P. Van Cappellen, Geological evolution of the marine selenium cycle: Insights from the bulk shale δ 82/76 Se record and isotope mass balance modeling. *Earth Planet. Sci. Lett.* **441**, 178–187 (2016).

73. P. A. E. Pogge von Strandmann, E. E. Stüeken, T. Elliott, S. W. Poulton, C. M. Dehler, D. E. Canfield, D. C. Catling, Selenium isotope evidence for progressive oxidation of the Neoproterozoic biosphere. *Nat. Commun.* **6**, (2015).

74. A. J. T. Shore, Selenium geochemistry and isotopic composition of sediments from the Cariaco Basin and the Bermuda Rise: A comparison between a restricted basin and the open ocean over the last 500 ka. Ph.D. thesis, University of Leicester, Leicester, UK (2010).

75. H. J. Wen, J. Carignan, X. L. Chu, H. F. Fan, C. Cloquet, J. Huang, Y. X. Zhang, H. J. Chang, Selenium isotopes trace anoxic and ferruginous seawater conditions in the Early Cambrian. *Chem. Geol.* **390**, 164–172 (2014).

76. M. Lissner, S. König, A. Luguet, P. J. le Roux, S. Schuth, A. Heuser, A. P. le Roex, Selenium and tellurium systematics in MORBs from the southern Mid-Atlantic Ridge (47–50°S). *Geochim. Cosmochim. Acta* **144**, 379–402 (2014).

77. J. M. Brenan, Se–Te fractionation by sulfide–silicate melt partitioning: Implications for the composition of mantle-derived magmas and their melting residues. *Earth Planet. Sci. Lett.* **422**, 45–57 (2015).

78. F. E. Jenner, E. H. Hauri, E. S. Bullock, S. König, R. J. Arculus, J. A. Mavrogenes, N. Mikkelson, C. Goddard, The competing effects of sulfide saturation versus degassing on the behavior of the chalcophile elements during the differentiation of hydrous melts. *Geochem. Geophys. Geosyst.* **16**, 1490–1507 (2015).

79. J. Labidi, P. Cartigny, Negligible sulfur isotope fractionation during partial melting: Evidence from Garrett transform fault basalts, implications for the late-veneer and the hadean matte. *Earth Planet. Sci. Lett.* **451**, 196–207 (2016).

80. K. R. Ludwig, Isoplot 3.71. Berkeley Geochronology Centre (2008).

81. C. J. Allègre, D. L. Turcotte, Implications of a two-component marble-cake mantle. *Nature* **323**, 123–127 (1986).

82. C. Hamelin, L. Dosso, B. B. Hanan, M. Moreira, A. P. Kositsky, M. Y. Thomas, Geochemical portray of the Pacific Ridge: New isotopic data and statistical techniques. *Earth Planet. Sci. Lett.* **302**, 154–162 (2011).

83. O. Rouxel, J. Ludden, J. Carignan, L. Marin, Y. Fouquet, Natural variations of Se isotopic composition determined by hydride generation multiple collector inductively coupled plasma mass spectrometry. *Geochim. Cosmochim. Acta* **66**, 3191–3199 (2002).

84. J. Labidi, S. König, T. Kurzawa, A. Yierpan, R. Schoenberg, The selenium isotopic variations in chondrites are mass-dependent; Implications for sulfide formation in the early solar system. *Earth Planet Sci. Lett.* **481**, 212–222 (2018).

85. W. F. Mcdonough, S.-S. Sun, The Composition of the Earth. *Chem. Geol.* **120**, 223–253 (1995).

86. Z. Wang, H. Becker, Ratios of S, Se and Te in the silicate Earth require a volatile-rich late veneer. *Nature* **499**, 328–331 (2013).

87. H. Palme, H. S. C. O'Neill, in *Treatise on Geochemistry (Second Edition),* H. D. Holland, K. K. Turekian, Eds. (Elsevier, Oxford, 2014), pp. 1–39.

88. V. J. M. Salters, A. Stracke, Composition of the depleted mantle. *Geochem. Geophys. Geosyst.* **5**, Q05B07 (2004).

89. T. Plank, in *Treatise on Geochemistry,* H. D. Holland, K. K. Turekian, Eds. (Elsevier, Oxford, 2014), pp. 607–629.

90. C. T. A. Lee, M. Erdman, W. B. Yang, L. Ingram, E. J. Chin, D. J. DePaolo, Sulfur isotopic compositions of deep arc cumulates. *Earth Planet. Sci. Lett.* **500**, 76–85 (2018).

91. R. L. Rudnick, S. Gao, in *Treatise on Geochemistry,* H. D. Holland, K. K. Turekian, Eds. (Pergamon, Oxford, 2003), pp. 1–64.

92. F. E. Jenner, Cumulate causes for the low contents of sulfide-loving elements in the continental crust. *Nat. Geosci.* **10**, 524–529 (2017).

93. W. Xu, J.-M. Zhu, T. M. Johnson, X. Wang, Z.-Q. Lin, D. Tan, H. Qin, Selenium isotope fractionation during adsorption by Fe, Mn and Al oxides. *Geochim. Cosmochim. Acta* **272**, 121–136 (2020).

94. G. H. Floor, G. Román-Ross, Selenium in volcanic environments: A review. *Appl. Geochem.* **27**, 517–531 (2012).

95. A. Gale, C. A. Dalton, C. H. Langmuir, Y. Su, J.-G. Schilling, The mean composition of ocean ridge basalts. *Geochem. Geophys. Geosyst.* **14**, 489–518 (2013).

96. A. Stracke, M. Bizimis, V. J. M. Salters, Recycling oceanic crust: Quantitative constraints. *Geochem. Geophys. Geosyst.* **4**, (2003).